

Tunable Nano-photonic Devices

By

Copyright 2016

Susobhan Das

Submitted to the graduate degree program in the Department of Electrical Engineering and Computer Science and the Graduate Faculty of the University of Kansas in partial fulfillment of the requirements for the degree of Doctor of Philosophy.

Chairperson Dr. Rongqing Hui

Co-Chairperson Dr. Alessandro Salandrino

Dr. Judy Z. Wu

Dr. James Stiles

Dr. Christopher Allen

Date Defended: <<12/06/2016>>

The Dissertation Committee for Susobhan Das
certifies that this is the approved version of the following dissertation:

Tunable Nano-photonic Devices

Chairperson Dr. Rongqing Hui

Co-Chairperson Dr. Alessandro Salandrino

Date approved: <<12/06/2016>>

Abstract

For high speed photonic systems and networks, encoding electronic signal onto optical carrier requires electro-optic modulators in which electromagnetic fields of the optical carrier can be manipulated electronically. The central focus of this research is twofold. First, tunable properties and tuning mechanisms of different optical materials like Graphene, Vanadium di-oxide, and Indium Tin Oxide are characterized systematically in telecommunication wavelength region. Then, these materials are implemented to design novel nano-photonic devices such as electro-optic modulators and tunable couplers with high efficiency and miniature footprint suitable for photonic integration.

Specifically, we experimentally investigated the complex index of graphene in near infrared wavelength through the reflectivity measurement on a SiO₂/Si substrate. The measured change of reflectivity as the function of applied gate voltage is highly correlated with theoretical modeling based on the Kubo formula. Based on a fiber-optic pump-probe setup we demonstrated that short optical pulses can be translated from pump wavelength to probe wavelength through dielectric-to-metal phase transition of vanadium di-oxide. In this process, pump leading edge induced optical phase modulation on the probe is converted into an intensity modulation through an optical frequency discriminator. We also theoretically modeled the permittivity of Indium Tin-Oxide with different level of doping concentration in near infrared region.

We proposed an ultra-compact electro-optic modulator based on switching plasmonic resonance “ON” and “OFF” of ITO-on-graphene via tuning of graphene chemical potential through electrical gating. The plasmonic resonance of ITO-on-graphene significantly enhances the electromagnetic field interaction with graphene which allows the reduction of modulator size compare to graphene based modulators without ITO. We presented a scheme of mode-

multiplexed near infrared modulator by tuning of ITO permittivity as the function of carrier density through externally applied voltage. The wisely patterned ITO on top of an SOI ridge waveguide portrayed the independent modulation of two orthogonal modes simultaneously, which enhances functionality per area for on-chip photonic applications. We proposed a theoretical model of tunable anisotropic metamaterial composed of periodic layers of graphene and Hafnium Oxide where transversal permittivity can be tuned via changing the chemical potential of graphene. A novel metamaterial assisted tunable photonic coupler is designed by inserting the proposed artificial tunable metamaterial in the coupling region of a parallel waveguide coupler. The coupling efficiency can be tuned by changing the permittivity of metamaterial through external electrical gating.

Acknowledgements

First of all, I would like to express my huge thank to my supervisors, Dr. Rongqing Hui, and Dr. Alessandro Salandrino. They provided me endless support and guidance over my past three years study in KU. Without their excellent advice, invaluable ideas and suggestions, and encouragement that I have received from them throughout my doctoral program, I won't be able to finish my PhD. I also want to thank Dr. Shima Fardad for enriching me with hands on experiments. I owed them so much that thank you is not enough to express my deep gratitude.

I would like to thank Dr. Judy Z. Wu, Dr. James Stiles, and Dr. Christopher Allen for serving on my dissertation committee and examining my research work

Table of Contents

Introduction & Literature Review	1
1.1. Motivation	1
1.2. Background of research.....	3
1.2.1. Optical Waveguide.....	3
1.2.2. Surface Plasmon Polariton.....	6
1.2.3. Drude model.....	11
1.3. Recent Technology.....	12
1.4. Overview of Proposed Work.....	22
1.4.1 Material Characterization.....	22
1.4.2 Photonic Devices	23
Material Characterization.....	24
2.1. Introduction	24
2.2. Graphene	25
2.2.1 Experimental Setup & Result.....	28
2.3. Indium Tin Oxide.....	33

2.4.	Vanadium di Oxide	35
2.4.1.	Experimental Setup and Results	37
2.5.	Conclusion.....	24
Photonic Devices.....		45
3.1.	Introduction	45
3.2.	NIR EOM based on plasmonic graphene.....	46
3.2.1	Device configuration and operation principle.....	48
3.2.2	Results and discussion	52
3.3.1	Device configuration and operation principle.....	61
3.3.2	Results and discussion	63
3.4.2	Device configuration and operation principle.....	71
3.4.3	Results and discussion	72
3.3.	Conclusion	24
Conclusion and future work		78
References.....		81

Chapter I:

Introduction & Literature Review

1.1. Motivation

In the era of nano-technology, novel single-chip multiprocessors with enhanced performances call for physical architectures supporting the ever increasing demands of clock speed, with a consequent increment in the complexity of these systems. As speed and complexity of these systems increase the interconnect density and throughput management becomes a critical factor towards the realization of high performance data processing systems. Currently copper interconnects are used for data transmission over chip-to-chip and chip-to-module interfaces, in chip-to-chip over backplane, and in chip-to-chip over copper cable assemblies. Because of ringing, increasing signal latency, crosstalk and frequency dependent attenuation, performance of Electrical interconnects degrades at frequencies above 1 GHz [1]. These limitations of electrical interconnects will limit the maximum frequency of operation for future systems. Optical interconnect is seen as a potential solution since it can directly address these problems at the system level and meet the performance requirements of current and future generation of data processors. Optical interconnects have negligible frequency dependent loss, low cross talk and high band width. Despite the significant interest shown by many groups worldwide, optical interconnects are not much used commercially. In order to become a viable technology to replace electrical-based on-chip interconnects, optical interconnects should be made compatible with manufacturing processes and assembly methods that are already in use in the semiconductor industry further there is a need to develop efficient and compact optical interconnect modules that use simple optical and electrical interfacing schemes. The development of optical

interconnects, especially based on a technology platform which is monolithically integratable into Si CMOS at low cost is needed in order to make optical interconnects economically viable. This will result in low cost, high performance and CMOS compatible optical components. Since it is not possible to make silicon light emitting and detecting we have to integrate other materials with Si. Large-scale integration of optical devices has been demonstrated on III-V platforms but in this implementation the components have different technology and they cannot be monolithically integrated on the same substrate. Monolithic integration of optical and electronic components on one substrate [2-7] together with demonstrations of efficient fiber to waveguide couplers [8] has shown the promise for development of ultra-compact optical components compatible with current technology. During the past decade several photonic-devices architectures have been developed. Silicon-based structures are certainly attractive from a technological point of view, however, due to the weak non-linear electro-optical properties of silicon, electro-optic modulators relying on silicon alone [9] require large device footprints on the orders of millimeters. The use of high-Q ring resonator structures [10, 11] has been shown to partially circumvent this problem, reducing the devices footprints to micron-size dimensions at the expense of the device bandwidth. Moreover, in silicon technology electromagnetic waves can't be confined below diffraction limit [12]. If the device size goes below diffraction limit, scattering phenomena dominates and as a consequence loss of the device enhanced by a lot [13, 14]. On the other hand, plasmonic effect has the capability to confine electromagnetic field below diffraction limit [15]. To get the appropriate resonance condition, the negative permittivity of the metal has to be comparable to the permittivity of the dielectric in the operating wavelength region [16]. As we are interested in NIR region, conventional metal such as gold (Au), silver (Ag), Copper (Cu) have very large negative permittivity (-100~ -200) compared to silicon dioxide,

hafnium di-oxide, aluminum oxide [17-19]. Therefore, characterizations of new materials with lower negative permittivity are highly required to achieve plasmonic resonance effect in NIR region. Combining plasmonic effect with photonic devices, it is possible to narrow down the device size further more with high speed operation.

1.2. Background of research

1.2.1. Optical Waveguide

Normally to guide optical signals, conventional structures such as optical fibers, planar waveguides, and ridge waveguides are customarily used. All of these optical waveguides consist of a core, in which light energy is confined, and a cladding or substrate surrounding the core as shown in figure 1.1.

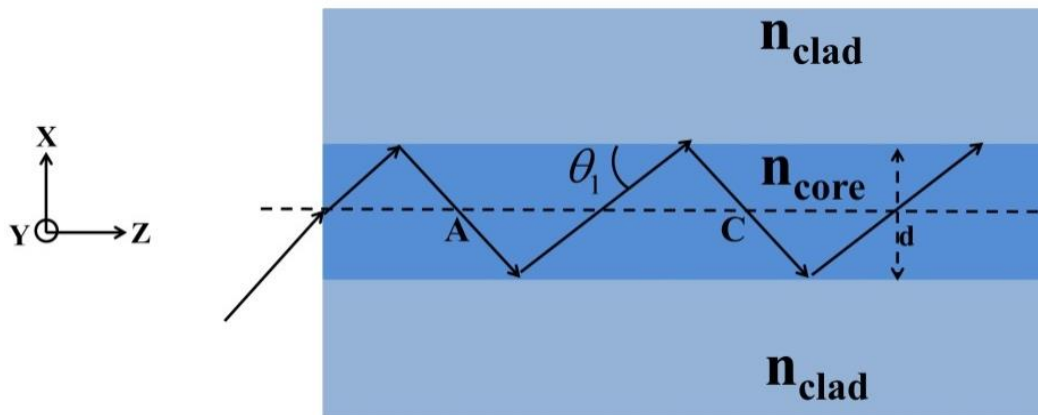


Figure: 1. 1. Basic Structure of optical waveguide

The refractive index of core n_{core} is higher than refractive index of cladding n_{clad} . Therefore the light beam that is coupled to the end face of the waveguide is confined in the core by total internal reflection. Condition for total internal reflection at core-cladding interface is given by equation 1.1.

$$\theta_1 \leq 90^\circ - \sin^{-1}\left(\frac{n_{clad}}{n_{core}}\right) \quad 1.1$$

But equation 1.1 is essential to confine light wave inside the core but not sufficient to form a guided mode. The phase accumulation for a full cycle of rebounded at the interface of core and cladding i.e. any two end points of full cycle of rebounded ray ‘A’ and ‘C’ has to be integral multiple of 2π . Therefore, sufficient condition for guided mode inside the core is given by equation 1.2.

$$\frac{2n_{core}kd}{\sin(\theta_1)} + 2\delta_1 = 2\pi M, M=1, 2, 3, \dots \quad 1.2$$

where, d is the width of the core, δ_1 is the phase change due to total internal reflection and k is free space propagation constant. To get the full field distribution of a mode, it is required to solve the wave equation for different structure of waveguides. Some conventional optical waveguide structures are shown in figure 1.2.

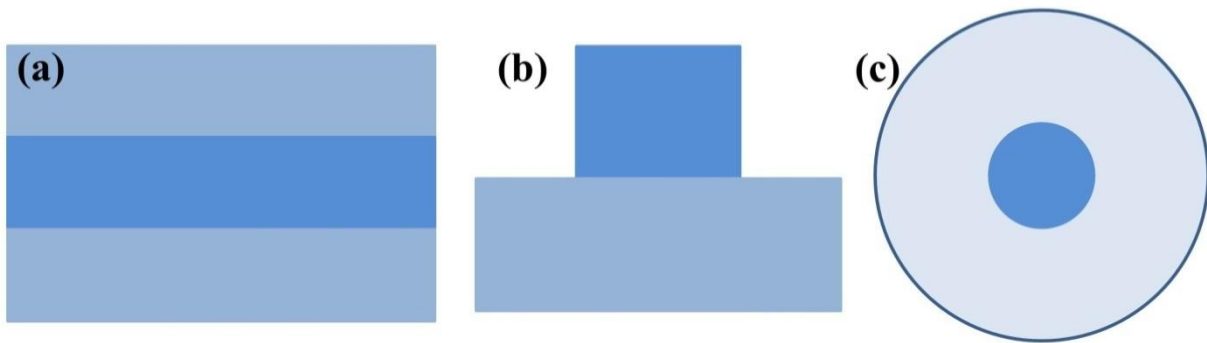


Figure: 1. 2. Different structure of optical waveguides (a) Planer waveguide, (b) Ridge waveguide, (c) Optical fiber

By solving wave equations given by equation 1.3, the solution of the wave equation depends on the coordinate system in which the waveguide is characterized [20-22].

$$\nabla^2 \vec{E} + \omega^2 \mu \epsilon \vec{E} = 0 \quad \text{for electric field}$$

1.3

$$\nabla^2 \vec{H} + \omega^2 \mu \epsilon \vec{H} = 0 \quad \text{for magnetic field}$$

Conventionally, for Cartesian coordinate system solution of the wave equations are sine or cosine function inside the core and exponential decay function for cladding or substrate area. For cylindrical coordinate system, field distributions are described by Bessel function of first kind in core region and by Bessel function of second kind in cladding region. Fundamental electric field distributions for three conventional waveguides are shown in figure 1.3.

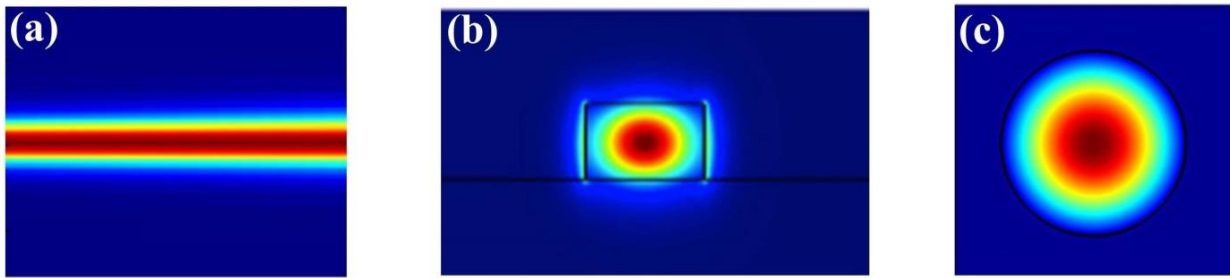


Figure: 1. 3. Normalized Electric field distribution of fundamental mode for (a) Planer waveguide, (b) Ridge waveguide, (c) Optical fiber

Convenient high speed data transmission thorough out the world is successfully implemented by optical fiber. To modulate the optical carrier signal with the data stream in a compact format for transmission and to recover the data at receiver end, requirement of high-speed optical devices like couplers, modulators detectors are ever in leading edge demand. Simultaneously, the space dependent complexity is also a main concern to enforce the silicon technology towards nano-photonics. On contrary, the diffraction limit builds an unbreakable wall to miniaturize silicon

devices. Surface plasmon polariton is one promising effect to break the wall of size limitation by confining electric field below diffraction limit.

1.2.2. Surface Plasmon Polariton

Plasma is one of the four fundamental states of matter (the others being solid, liquid, and gas). Acquiring energy a gas may ionize its molecules or atoms (reducing or increasing the number of electrons in them), thus turning it into plasma, which contains charged particles: positive ions and negative electrons or ions. A plasmon is a quantum of plasma oscillation. Plasmon exists mainly in metals, where electrons are weakly bound to atoms and free to roam around. The electrons in a metal can wobble like a piece of jelly, pulled back by the attraction of positive metal ions that they leave behind. In contrast to the single electron wave function, a plasmon is a collective wave where billions of electrons oscillate in synchronous way. So, plasmons are collective oscillations of the free electron gas density. Plasmonics deals with solid-state structured or composite conductors, and their interaction with an electromagnetic radiation.

Surface plasmon polariton (SPP) are electromagnetic excitations propagating at the interface between a dielectric and a conductor, evanescently confined in the perpendicular direction. These electromagnetic surface waves arise via coupling of the electromagnetic fields to oscillations of the conductor's electron plasma.

The simplest geometry sustaining SPPs as shown in figure 1.4 is a single flat interface between a dielectric, non-absorbing half space ($Z > 0$) with positive real dielectric constant ϵ_d and an adjacent conducting half space ($Z < 0$) described via dielectric constant ϵ_m .

At the interface between metal and dielectric there will be TM or TE mode solutions. First considering TM solution, wave equation for TM modes is given by equation 1.4.

$$\frac{\partial^2 H_y}{\partial z^2} + (k_0^2 \epsilon - \beta^2) H_y = 0 \quad 1.4$$

Field distribution for $Z < 0$

$$\begin{aligned} H_y(z) &= A_1 e^{i\beta x} e^{k_1 z} \\ E_x(z) &= -iA_1 \frac{1}{\omega \epsilon_0 \epsilon_m} k_1 e^{i\beta x} e^{k_1 z} \\ E_z(z) &= -A_1 \frac{\beta}{\omega \epsilon_0 \epsilon_m} e^{i\beta x} e^{k_1 z} \end{aligned} \quad 1.5$$

For $Z > 0$ field distribution is given by

$$\begin{aligned} H_y(z) &= A_2 e^{i\beta x} e^{-k_2 z} \\ E_x(z) &= -iA_2 \frac{1}{\omega \epsilon_0 \epsilon_d} k_2 e^{i\beta x} e^{-k_2 z} \\ E_z(z) &= -A_2 \frac{\beta}{\omega \epsilon_0 \epsilon_d} e^{i\beta x} e^{-k_2 z} \end{aligned} \quad 1.6$$

k_1 and k_2 are components of wave vectors perpendicular to the interface in the two medium. Its reciprocal value, $z = 1/|k_z|$, defines the evanescent decay length of the fields perpendicular to the interface which quantifies the confinement of the wave. The continuity of tangential electric and magnetic field [23] at the interface leads to equality given by equation 1.7.

$$A_1 = A_2 \quad 1.7$$

$$\frac{k_2}{k_1} = -\frac{\epsilon_d}{\epsilon_m}$$

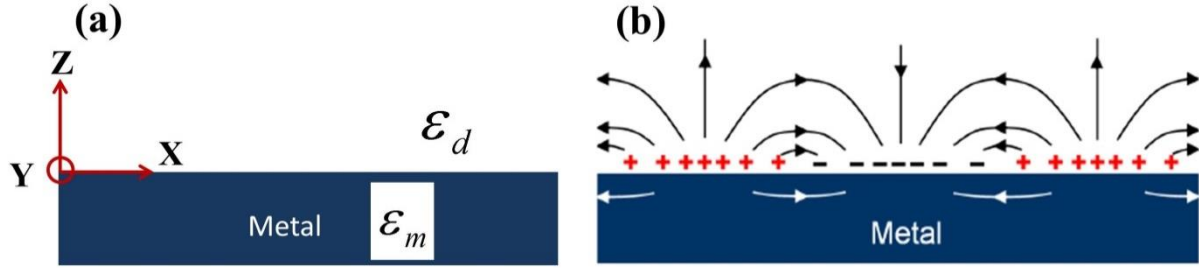


Figure: 1. 4. (a) Schematic diagram of metal dielectric interface and (b)electric field distribution for SPP

$k_2/k_1 > 0$ and $\epsilon_d > 0$; therefore to satisfy the condition $\text{Re}[\epsilon_m] < 0$ is necessary. In conclusion, the surface waves exist only at interfaces between materials with opposite signs of real part of their dielectric permittivity i.e. between a conductor and an insulator. The expression H_y further satisfied the wave equation 1.4 leads to equation 1.7.

$$k_1^2 = \beta^2 - k_0^2 \epsilon_m \quad 1.8$$

$$k_2^2 = \beta^2 - k_0^2 \epsilon_d$$

Combining equation 1.7 and equation 1.8, the dispersion relation of SPPs propagating at the interface between two half spaces is given by

$$K_{SPP} = \frac{\omega}{c} \sqrt{\frac{\epsilon_d \epsilon_m}{\epsilon_d + \epsilon_m}} \quad 1.9$$

This expression is valid for both real and complex permittivity of metal. The electric field distribution for SPP at the metal dielectric interface is shown in figure 1.4(b). The graphical representation of dispersion equation 1.9 for SPP is presented in figure 1.5, where ω_p is the plasma frequency of metal derived from the Drude Model. For the regime $\omega > \omega_p$, the metal becomes transparent in these frequencies. The electromagnetic field is then oscillating inside the metal, and it is known as radiation plasmon polariton (RPP) region [24].

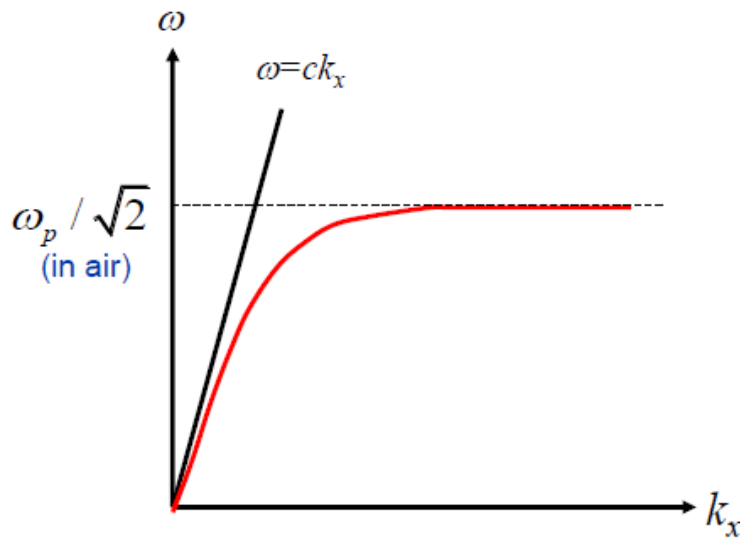


Figure: 1. 5. Dispersion relation for SPP at metal dielectric interface (red solid line).

It can be seen that the wave vector k_x goes to infinity and the group velocity goes to zero as the plasmon approaches ω_{sp} . This ω_{sp} is the classical, nondispersive surface plasmon (SP) frequency defined by [25].

$$\omega_{sp} = \sqrt{\frac{\omega_p}{1 + \epsilon_d}} \tag{1.10}$$

In this regime, the propagation constant $\beta = k_x n$ is much larger than the plasma frequency of the metal $k_x \gg \omega_p / c$, k_1 and k_2 become more equal. As a result, the SPP condition (1.7) simplifies to $\epsilon_m = -\epsilon_d$. This implies a non-propagating collective vibration of electron cloud near the metal interface. The resulting electrostatic mode is known as SP [26].

For TE modes, wave equation is given by

$$\frac{\partial^2 E_y}{\partial z^2} + (k_0^2 \epsilon - \beta^2) E_y = 0 \quad 1.11$$

Field distribution for $Z < 0$

$$\begin{aligned} E_y(z) &= A_1 e^{i\beta x} e^{-k_1 z} \\ H_x(z) &= iA_1 \frac{1}{\omega \mu_0} k_1 e^{i\beta x} e^{k_1 z} \\ H_z(z) &= A_1 \frac{\beta}{\omega \mu_0} e^{i\beta x} e^{k_1 z} \end{aligned} \quad 1.12$$

For $Z > 0$ field distribution is given by

$$\begin{aligned} E_y(z) &= -A_2 e^{i\beta x} e^{-k_2 z} \\ H_x(z) &= iA_2 \frac{1}{\omega \mu_0} k_2 e^{i\beta x} e^{-k_2 z} \\ H_z(z) &= -A_2 \frac{\beta}{\omega \mu_0} e^{i\beta x} e^{-k_2 z} \end{aligned} \quad 1.13$$

Continuity of E_x and H_y at the interface leads to the condition $A_1(k_1 + k_2) = 0$. Since confinement to the surface requires $k_1, k_2 > 0$, this condition is only fulfilled if $A_1 = 0$ so that $A_2 = A_1 = 0$. Thus no surface mode exists for TE polarization. Surface Plasmon Polariton only exists for TM polarization.

1.2.3. Drude model

The Drude model takes a macroscopic view of charge carrier (electron or hole) motion, using a simple equation of motion and deriving the material permittivity. In the Drude model, metals are characterized by a cloud of free electrons that are not bound to a particular atomic nucleus but are free to move about within the metal lattice. The model also includes frictional damping that describes the resistance to movement felt by the electrons. This damping arises from collisions within the lattice between moving electrons and positive, stationary ions. Therefore the equation of motion written as [27]

$$m_e \frac{\partial^2 r(t)}{\partial t^2} + m_e \Gamma \frac{\partial r(t)}{\partial t} = e E e^{-i\omega t} \quad 1.14$$

Where e , m are the charge and mass of electron and E and ω are the amplitude and frequency of the incident electric field. The damping term is proportional to the $\Gamma = v_f / l$, where v_f is the fermi velocity and l is the mean free path between scattering events. The solution of equation 1.14 is given by

$$r(t) = \frac{e}{m_e (\omega^2 + i\Gamma \omega)} E e^{-i\omega t} \quad 1.15$$

The microscopic polarization $P = -Ner$ which is related to $D = \epsilon_0 E + P$. From these relations permittivity of metal can be represented as

$$\begin{aligned}\epsilon_m &= 1 - \frac{\omega_p^2}{\omega^2 + i\omega\Gamma} \\ \omega_p &= \sqrt{\frac{Ne^2}{\epsilon_0 m_e}}\end{aligned}\tag{1.16}$$

where ω_p is the plasma frequency, N is free carrier density.

1.3. Recent Technology

The ultra-compactness of photonic devices has reached a bottleneck due to diffraction limit. New approaches that can confine the electromagnetic waves in subwavelength scale to miniaturize the entire photonic circuit, are highly essential. Plasmonics, which combines nanoscale light confinement and optical-speed processing of signals, has potential to enable the next generation of hybrid information-processing devices, which are superior to the current photonic dielectric components in terms of speed and compactness. Among all these new generation of optical devices, modulator is the prime component for digital signal encoding. The development of nanophotonic circuitry depends greatly on advance in modulator schemes configurations. A few advance design schemes are briefly described here.

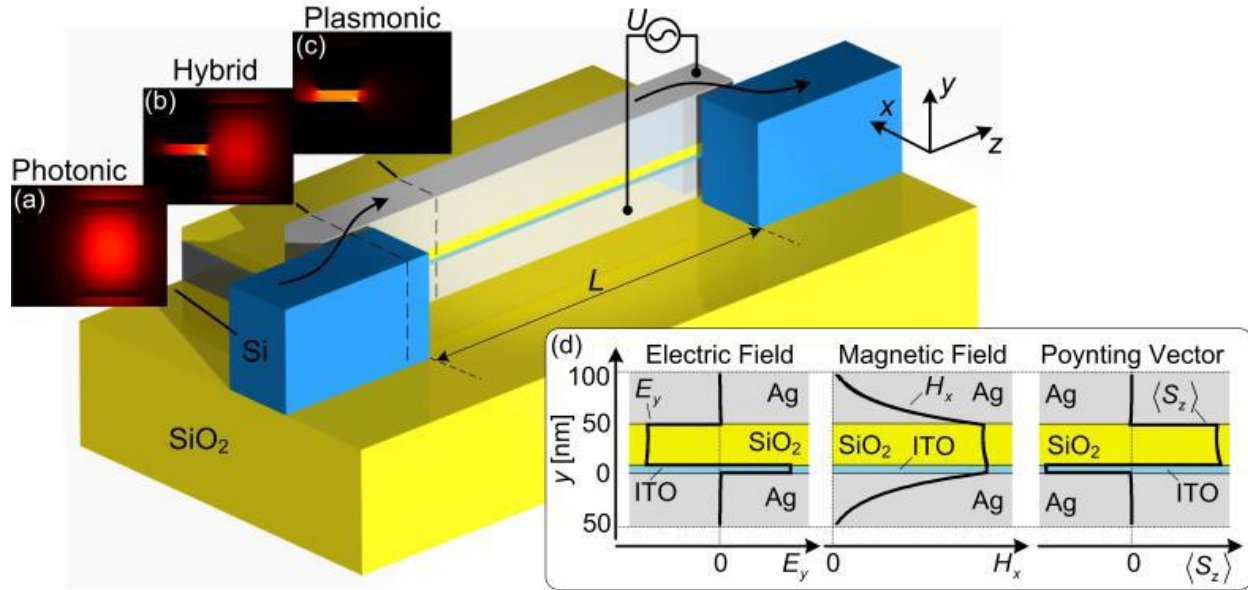


Figure: 1. 6. Schematic view of the horizontally arranged silicon-based plasmonic electro-absorption modulator [28]

An electrically controlled ultra-compact surface plasmon polariton absorption modulator (SPPAM) [28] is shown in figure 1.6. The absorption modulator comprises a stack of metal / insulator / metal-oxide / metal layers, which support a strongly confined asymmetric surface plasmon polariton (SPP) in the 1.55 μm telecommunication wavelength window. The transformations from photonic mode guided by the silicon waveguide to the plasmonic mode supported by designed modulator and vice versa are carried out through a hybrid section for better confinement and higher efficient modulation. The modulator section of the device can be as small as a few micrometers depending on the required extinction ratio and the acceptable loss. The device allows for operation far beyond 100 Gbit / s, being only limited by RC time constants. Absorption modulation is achieved by electrically modulating the free carrier density in the intermediate metal-oxide layer.

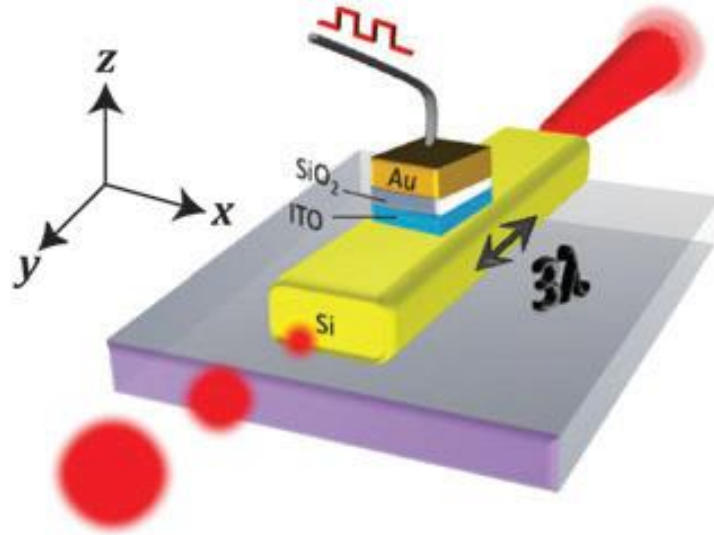


Figure: 1. 7. Schematic of the ultra-compact, waveguide-integrated, silicon-based nanophotonic modulator. Electrical data become encoded on an optical beam via the electroabsorption effect. The MOS design features a plasmonic optical mode which concentrates the mode's electric field and allows for a good overlap with the active ITO layer; in short gives rise to enhanced light-matter-interactions [29].

Another schematic of Electro-optic modulators as shown in figure 1.7, have been designed and experimentally demonstrated by Zhang group, the University of California, Berkeley [29]. The experimental observation demonstrated that the ultra-compact, silicon-based, electro-optic modulator has a record-high 1 dB per micrometer extinction ratio over a wide bandwidth range of 1 μm in ambient conditions. The device is based on a plasmonic metal-oxide-semiconductor (MOS) waveguide, which efficiently concentrates the optical modes' electric field into a nanometer thin region comprised of an absorption coefficient-tuneable indium-tin-oxide (ITO) layer. The modulation mechanism originates from electrically changing the free carrier concentration of the ITO layer which dramatically increases the loss of this MOS mode. The seamless integration of such a strong optical beam modulation into an existing silicon-on-

insulator platform bears significant potential towards broadband, compact and efficient communication links and circuits.

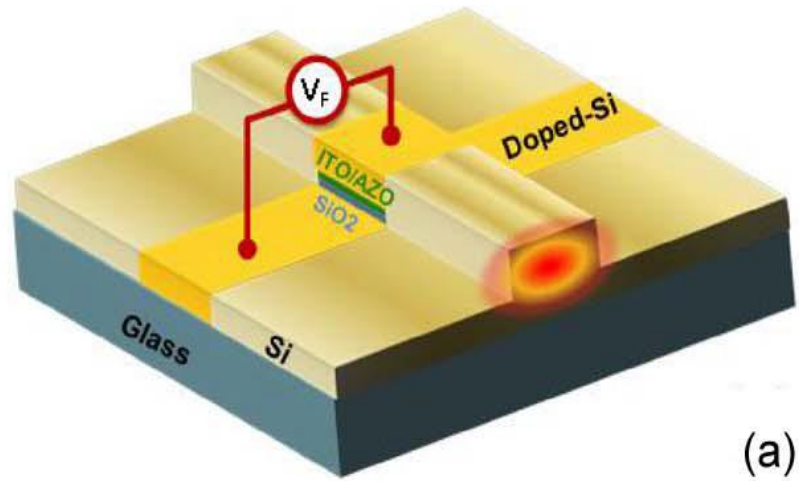


Figure: 1. 8. The illustration of an EA modulator embedded on a rib Si waveguide [30].

Lu group of the Rochester Institute of Technology presents a promising application of epsilon-near-zero (ENZ) materials in optical modulators [30]. When a thin ENZ film is sandwiched in a single-mode waveguide, an ENZ-slot waveguide is formed, where the absorption can be greatly enhanced. The schematic diagram of the proposed electro-absorption modulators based on tunable ENZ materials and slot waveguides is described in figure 1.8. Transparent conducting oxides (TCOs) may be employed as the active slot, which can be tuned between ENZ (high absorption) and epsilon-far-from-zero (low absorption) by accumulation carriers. Numerical simulation shows that over 3-dB modulation depth can be achieved in a 250-nm-long TCO-slot waveguide. The modulators have the advantages of nanoscale footprints, small insertion loss, potentially ultrahigh speed, and easy fabrication.

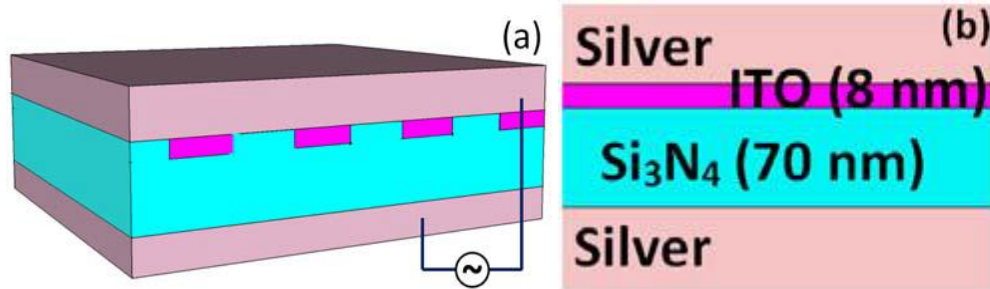


Figure: 1. 9. The improved modulator design with periodic ITO stripes. b) Schematic two dimensional view of the equivalent four-layer system [31].

An ultra-compact plasmonic modulator that can be applied in photonic integrated circuits has been theoretically demonstrated by V. E. Babicheva and A. V. Lavrinenko as schematic is depicted in figure 1.9 [31]. The modulator is a metal-insulator-metal waveguide with an additional ultra-thin layer of indium tin oxide (ITO). Bias is applied to the multilayer core by means of metal plates that serve as electrodes. External field changes carrier density in the ultra-thin ITO layer, which influences the permittivity. The metal-insulator-metal system possesses a plasmon resonance, and it is strongly affected by changes in the permittivity of the active layer. The substitution of the continuous active layer by a one-dimension periodic stripes increases transmittance through the device and keeps the modulator's performance at the same level. Patterned ITO layers offer a Bragg grating inside the waveguide, which can be turned on and off by application of externally applied voltage, thus modulating reflection from the structure.

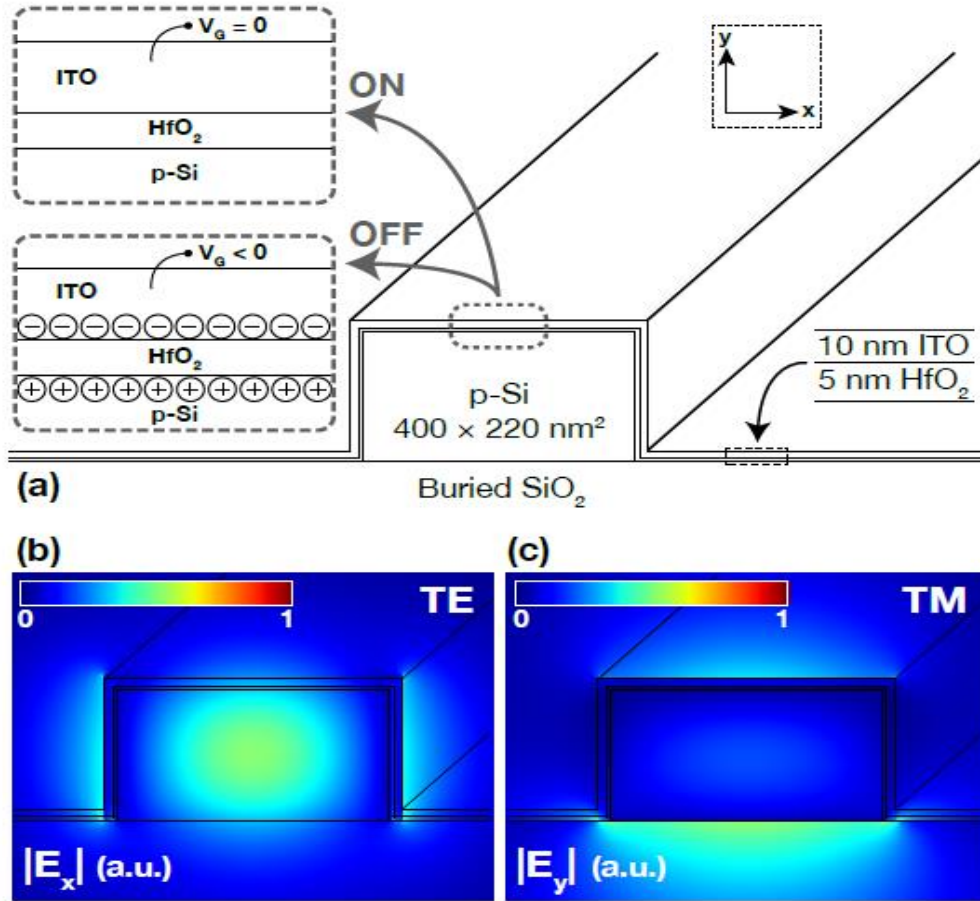


Figure: 1. 10. The proposed modulator consists of a silicon-on-insulator (400220nm²) waveguide coated with layers of HfO₂ (5 nm) and ITO (10 nm), forming a MOS capacitor (a). Without an applied bias, the ITO absorbs little light leading to a highly transmissive ON state (upper inset). With a negative bias between the ITO and the Si, an electron accumulation layer is induced at the ITO-HfO₂ interface. This accumulation layer modifies ITO's local optical permittivity, creating an epsilon-near-zero (ENZ) region that perturbs the waveguide mode into a highly absorptive OFF state (lower inset). This electro-absorption modulation occurs for both TE-like and TM-like modes supported by the waveguide structure (b), (c). The TE (TM) mode exhibits discontinuities in jE_x (jE_y) at interfaces due to dielectric constant mismatches [32].

Another scheme of optical electro-absorptive modulation based on accumulation of electrons in transparent conductive oxides for both TE and TM polarization has been proposed by Geballe Laboratory for Advanced Materials, Stanford University [32]. Accumulating electrons in

transparent conductive oxides such as indium tin oxide (ITO) can induce an "epsilon-near-zero" (ENZ) in the spectral region near the important telecommunications wavelength of $\lambda = 1.55\mu\text{m}$. This modulator leverages the combination of a local electric field enhancement and increased absorption in the ITO when this material is locally brought into an ENZ state via electrical gating. This leads to large changes in modal absorption upon gating. It is reported that a 3 dB modulation depth can be achievable in a non-resonant structure with a length under $30\mu\text{m}$ for the fundamental waveguide modes of either linear polarization, with absorption contrast values as high as 37.

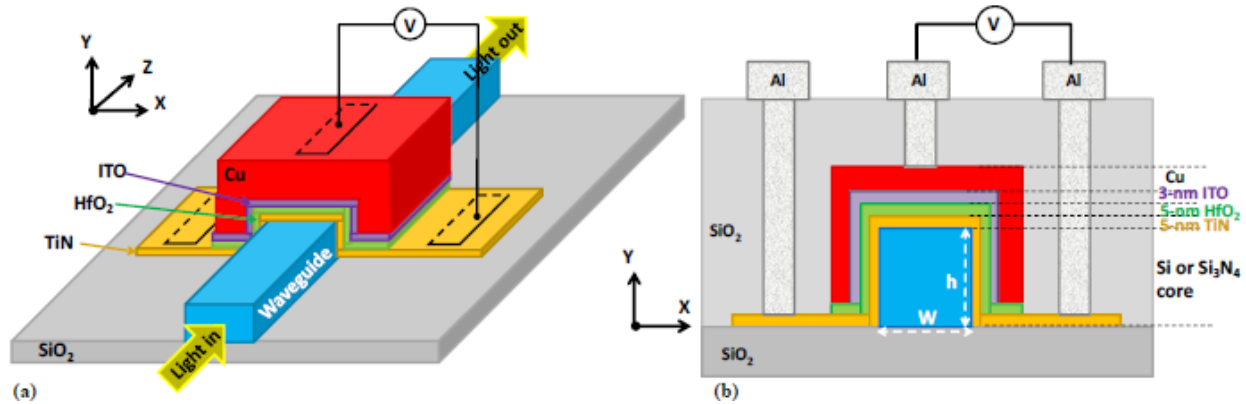


Figure: 1. 11. (a) 3D view and (b) cross-sectional view of the proposed EA modulator integrated with a stripe dielectric waveguide [33].

An ultra-compact electro-absorption (EA) modulator comprised of a stack of TiN/HfO₂/ITO/Cu conformally deposited on a single-mode stripe waveguide to form a hybrid plasmonic waveguide (HPW), operating around 1.55- μm telecom wavelengths is proposed and theoretically investigated by A. Zhu *et. al.* as shown in figure 1.11 [33]. Since the thin ITO layer can behave as a semiconductor, the stack itself forms a MOS capacitor. A voltage is applied between the Cu and TiN layers to change the electron concentration of ITO, which in turn changes its permittivity as well as the propagation loss of HPW. Optimizing the thickness of different layers

on a $400\text{-nm} \times 340\text{-nm}$ -Si stripe waveguide, the propagation loss for the $1.55\text{-}\mu\text{m}$ TE (TM) mode increases from 1.6 (1.4) to 23.2 (23.9) $\text{dB}/\mu\text{m}$ when the average N_{ITO} in the ITO layer increases from 2×10^{20} to $7 \times 10^{20} \text{ cm}^{-3}$, which is achieved by varying the voltage from -2 to 4 V if the initial N_{ITO} is $3.5 \times 10^{20} \text{ cm}^{-3}$. As a result, a $1\text{-}\mu\text{m}$ -long EA modulator inserted in the $400\text{-nm} \times 340\text{-nm}$ -Si stripe waveguide exhibits insertion loss of 2.9 (3.2) dB and modulation depth of 19.9 (15.2) dB for the TE (TM) mode. The modulation speed is ~ 11 GHz, limited by the RC delay, and the energy consumption is ~ 0.4 pJ/bit.

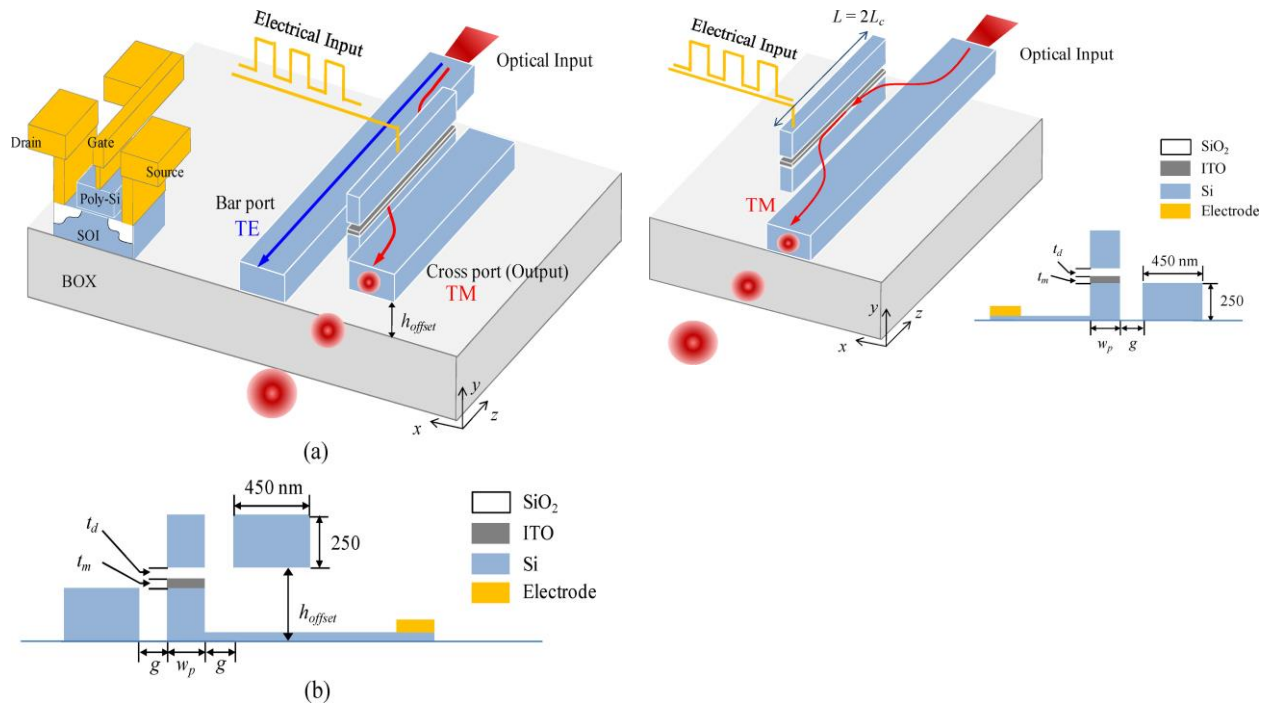


Figure: 1. 12. Schematic views of the proposed silicon optical modulator based on tunable three-core hybrid plasmonic directional couplers. (a) Bird's eye view and (b) cross sectional view of the coupler section. (c) Schematic bird-eye view of the Si optical modulator based a tunable two-core hybrid plasmonic coupler. The right figure is the cross-sectional view. The length of the hybrid plasmonic waveguide is $L = 2L_c$ [34].

waveguide with TiO_2/ITO layers on both sides of the InGaAsP core as shown in figure 1.13. Using this design, the intensity of transmitted light can be modulated by controlling the carrier concentration of the ITO layer, as a positive gate voltage induces electron accumulation in the ITO layer. The theoretical extinction ratio of the proposed device is $4.5\text{dB}/\mu\text{m}$ with a gate voltage swing of 0–5, and the insertion loss is found to be $1.5\text{dB}/\mu\text{m}$.

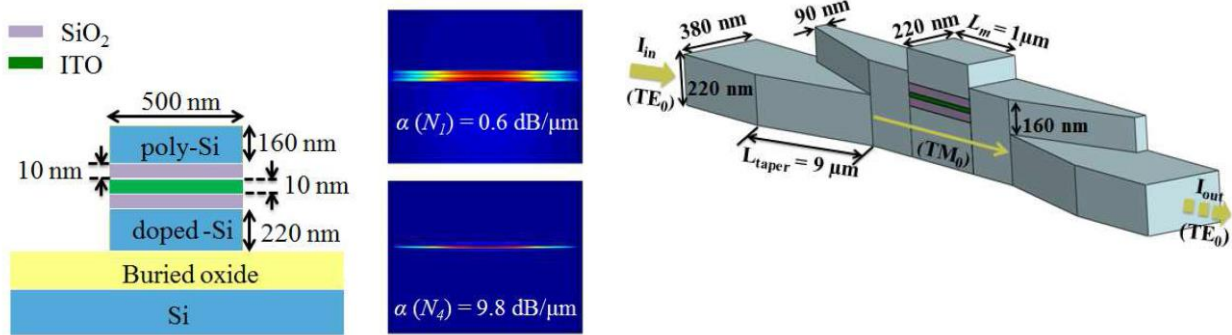


Figure: 1. 14. (a) Schematic of the modulator structure and the profiles of the fundamental TM mode ($\lambda = 1310 \text{ nm}$); (b) Three-dimensional schematic of the slot-waveguide modulator (with 7-nm thick Si_3N_4 buffers) butt coupled to Si strip waveguides [36].

H. Zhao *et.al.* from the Boston University proposed a compact silicon (Si) electro-absorption modulator based on a slot waveguide with epsilon-near-zero indium tin oxide materials as shown in figure 1.14 [36]. In order to integrate the device with low-loss Si strip waveguides, both butt-coupling and evanescent-coupling schemes are investigated. For both cases, our electro-absorption modulator demonstrates a high extinction ratio and a low insertion loss over a wide optical bandwidth for both TE and TM polarized modes.

1.4. Overview of Proposed Work

The focus area of the research work is the characterization of different materials theoretically and experimentally in NIR region; and design Si-based photonic devices with implementing those materials for various applications.

1.4.1 Material Characterization

The complex refractive index of graphene fabricated using chemical vapor deposition is characterized at 1550nm wavelength through the reflectivity measurement on a SiO₂/Si substrate. The observed tunability of the complex reflective index as the function of gate electric voltage is in agreement with the prediction based on the Kubo formula.

Indium Tin Oxide (ITO) is one of the promising transparent conducting oxides with low loss in NIR region comparing to the conventional plasmonic material like gold or silver. Moreover, permittivity of ITO can be tuned with changing of doping concentration. The mathematical modeling of permittivity of ITO is discussed with the help of Drude Model.

VO₂ is a promising material for reconfigurable photonic devices due to the ultrafast changes in electronic and optical properties associated with its dielectric-to-metal phase transition. Based on a fiber-optic pump-probe setup at 1550nm wavelength window, and by varying the pump pulse duration, we show that the material phase transition is primarily caused by the pump pulse energy. For the first time, we demonstrate that the instantaneous optical phase modulation of probe during pump leading edge can be utilized to create short optical pulses at probe

wavelength, through optical frequency discrimination. This circumvents the impact of long recovery time well-known for the phase transition of VO₂.

1.4.2 Photonic Devices

We propose a novel scheme for an electro-optic modulator based on plasmonically enhanced graphene. As opposed to previously reported designs where the switchable absorption of graphene itself was employed for modulation, here a graphene monolayer is used to actively tune the plasmonic resonance condition through the modification of interaction between optical field and an indium tin oxide (ITO) plasmonic structure. Strong plasmonic resonance in the near infrared wavelength region can be supported by accurate design of ITO structures, and tuning the graphene chemical potential through electrical gating switches on and off the ITO plasmonic resonance. This provides much increased electro-absorption efficiency as compared to systems relying only on the tunable absorption of the graphene.

As the diffraction limit is approached, device miniaturization to integrate more functionality per area becomes more and more challenging. Here we propose a novel strategy to increase the functionality-per-area by exploiting the modal properties of a waveguide system. With such approach the design of a mode-multiplexed nanophotonic modulator relying on the mode-selective absorption of a patterned Indium-Tin-Oxide is proposed. Full-wave simulations of a device operating at the telecom wavelength of 1550nm show that two modes can be independently modulated, while maintaining performances in line with conventional single-mode ITO modulators reported in the recent literature. The proposed design principles can pave the way to a novel class of mode-multiplexed compact photonic devices able to effectively multiply the functionality-per-area in integrated photonic systems.

Chapter II:

Material Characterization

A material consists of number of atoms or molecules oriented in a particular fashion. In the presence of oscillatory electromagnetic fields, the combine behavior of atoms or molecules represents the overall characteristics of the material. On the mark, the frequency of the oscillatory electromagnetic fields plays a great role on material properties. Therefore the characterization of different material in a particular frequency band is first and foremost fundamental requirement to implement them in device level.

2.1. Introduction

Normally, plasma frequency of the available noble metals like gold (Au), silver (Ag), aluminum (Al), and copper (Cu) are in very high frequency region nearly violate regime. Therefore, the real part of permittivity of those metals possess very high negative value (-100 ~ -200) at the optical communication range i.e. wavelength range from 15mm to 1.6 mm. To achieve plasmonic resonance effect, with those metals, the positive dielectric constant of the surrounding material has to be comparable to metals. It's very rare to achieve a very high positive permittivity in the communication window. On the contrary, there are groups of materials which behave as metal with low negative permittivity unfold the opportunity to achieve plasmonic resonance in NIR region with most available dielectric like silicon (Si), silicon dioxide (SiO₂), hafnium dioxide (HfO₂) etc. Moreover, the metallic characteristics of those materials can be modified or tuned electrically, optically and thermally.

To deploy those tunable materials in photonic devices, it is required to characterize the optical behavior of those materials with various conditions. Here we characterize three different

materials graphene, Indium Tin Oxide (ITO) and Vanadium dioxide (VO_2), which we use to build tunable photonic devices.

2.2. Graphene

Composed of a single layer of carbon atoms with honeycomb lattice, graphene is a promising two-dimensional material for many potential applications in electronics and photonics. The low-energy band structure of graphene can be described by a pair of Dirac cones [37-38]. At absolute zero temperature, the Fermi energy is at the charge neutrality point (Dirac point) where the lower energy cone is completely filled while the upper one is empty. Owing to the low density of states, the chemical potential in graphene can be modulated by an external gate voltage to populate electrons to the upper cone or deplete electrons from the lower cone. Thus, the tunability of chemical potential is a key to electrically regulating the optical transition of graphene-based devices. The excellent electrical properties of graphene, such as high carrier mobility and electrical conductivity, have been well studied and applied to build high-frequency field-effect transistors (FETs) [39]. The unique optical properties of graphene have been applied to create gas sensors [40], plasmonic resonators in terahertz [41] and electro-absorption optical modulators at 1550 nm wavelength [42]. Very recently, a variety of graphene based photonic nanostructures and devices have been theoretically proposed for operation in the optical communication wavelengths based on the tunable nature of graphene complex refractive index [43-44]. Thus, to bridge the gap between models and device realization, it is essential to accurately evaluate the refractive index of graphene at 1550 nm wavelength as the function of chemical potential. Most characterizations of graphene dielectric constant have been so far in visible [45], mid-infrared [38] and terahertz [41] wavelength ranges. We report here that the

voltage-dependent reflectivity at 1550 nm wavelength measured on a back-gated chemical vapor deposition-derived (CVD) graphene on SiO₂/Si substrate is in agreement with the calculated result based on the Kubo formula [46]. Hysteresis of reflectivity in response to the sweep of the applied gate voltage is also observed due to the process of charge trapping and storage in graphene.

The complex conductivity of monolayer graphene can be calculated using the well-known Kubo's formula [46]:

$$\sigma(\omega, \mu_c, \Gamma, T) = \frac{je^2(\omega - j2\Gamma)}{\pi\hbar^2} \left\{ \frac{1}{(\omega - j2\Gamma)^2} \int_0^\infty \left[\frac{\partial f_d(\varepsilon)}{\partial \varepsilon} - \frac{\partial f_d(-\varepsilon)}{\partial \varepsilon} \right] d\varepsilon - \int_0^\infty \left[\frac{f_d(\varepsilon) - f_d(-\varepsilon)}{(\omega - j2\Gamma)^2 - 4\left(\frac{\varepsilon}{\hbar}\right)^2} \right] d\varepsilon \right\} \quad (2.1)$$

which is the combination of the inter-band and intra-band absorptions represented by the 1st and the 2nd term, respectively, in Eq.(2.1). ω is the optical frequency, e is the electron charge, $\hbar = h/2\pi$ is the reduced Planck's constant, $f_d(\varepsilon) = 1/(e^{(\varepsilon - \mu_c)/k_B T} + 1)$ is the Fermi-Dirac distribution function. ε is the energy, k_B is the Boltzmann's constant, T is the absolute temperature, $\hbar\Gamma = 5meV$ is the scattering parameter [34], and μ_c is the chemical potential. The conductivity predicted by Eq.(1) can be converted into an in-plane complex refractive index: $n_g = \sqrt{1 - j\sigma/(\omega\varepsilon_0\delta_g)}$, where ε_0 is the free space permittivity, and $\delta_g = 0.34nm$ is the thickness of monolayer graphene. At 1550 nm optical communications wavelength, the refractive index of graphene as the function of chemical potential is shown in Fig.2.1, where the imaginary part n_i is primarily responsible for optical absorption.

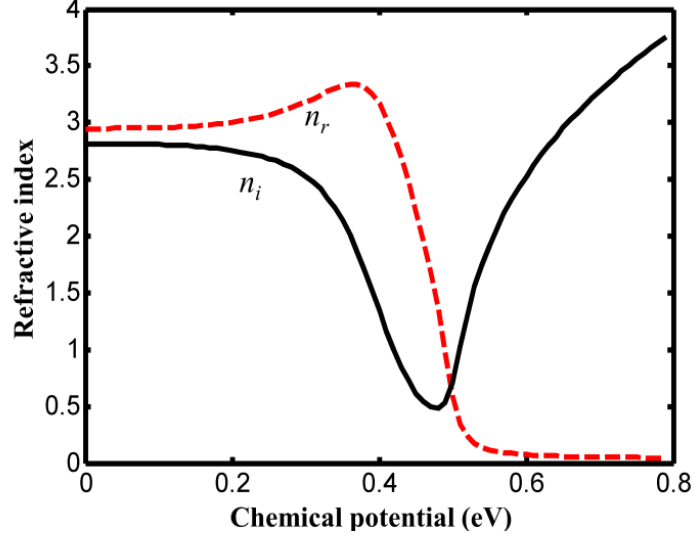


Figure: 2. 1. In-plane refractive index of graphene as the function of chemical potential at 1550 nm wavelength.

m_c is the chemical potential which is determined by charge accumulation on the graphene. The value of m_c can be varied by an applied gate voltage V through the silicon oxide capacitance between the graphene and the silicon substrate as,

$$\mu_c = \hbar v_F \sqrt{\frac{\pi \epsilon_{ox}}{e d_{ox}} (V - V_D)} \quad (2.2)$$

Where, e_{ox} and d_{ox} are the dielectric constant and the thickness of SiO_2 layer, and V_D is the Dirac voltage determined by the unintentional doping of the graphene from the substrate and its surrounding environment. $v_F \approx 0.75 \times 10^6 \text{ m/s}$ is the Fermi velocity [29], which was found to be dependent on the property of the substrate [47].

2.2.1 Experimental Setup & Result

Figure 2.2 shows the experimental setup. A fiber pigtailed laser diode at 1550 nm wavelength was used in the experiment with spectral linewidth of approximately 10 MHz. The laser output was collimated into the system and focused on the sample through a 20x objective lens, and the spot diameter on the sample was typically about $5\mu\text{m}$. The light reflected from the sample was collected through a 50% beam splitter and detected by a photodetector. A microscope was inserted in the optical system to observe the position of the light spot on graphene sample. A lock-in amplifier was used to improve the signal-to-noise ratio. Optical signal modulation for synchronizing the lock-in amplifier could be applied either through a mechanical chopper in front of the photodetector, or through a modulation on the gate voltage of the sample. A computer was used to control the motion of the translation stage, to adjust the gate voltage, and to acquire data from the lock-in amplifier.

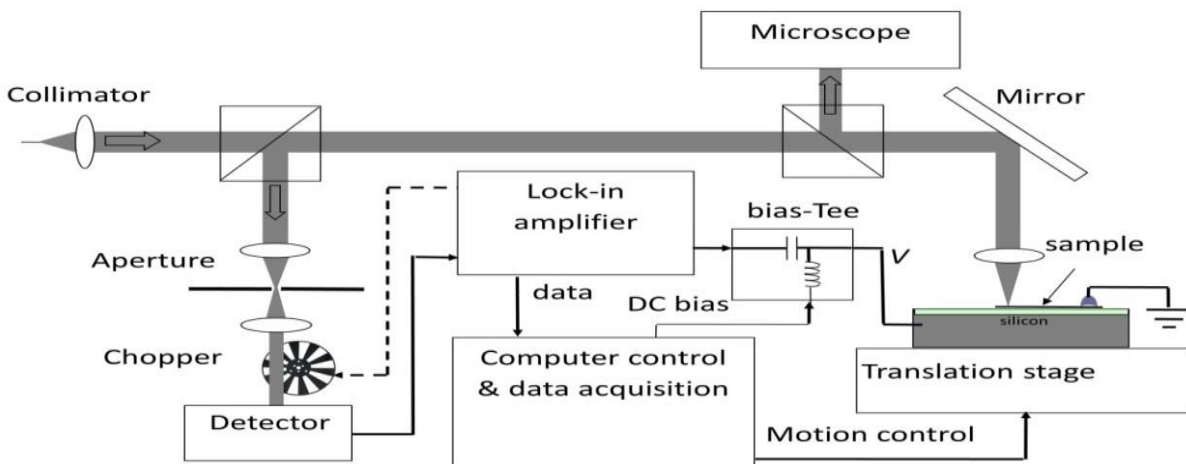


Figure: 2. 2. Experimental setup for graphene characterization

Fig. 3 shows the normalized reflectivity as the function of the beam position with the laser beam scanning across the edge of the graphene with zero gate voltage. In this measurement, lock-in amplifier was synchronized with the mechanical chopper in front of the photodetector. This allowed the measurement of reflectivity change from the sample surface when the laser beam scanned across areas with and without the graphene, which is approximately 1.1% as shown in Figure 2.3.

To confirm the repeatability of the measurement, the laser beam was scanned both in the forward and backward directions along the same line and the results are almost identical. The sharp notch of reflectivity measured at the graphene edge shown in Fig.3 was attributed to the unavoidable fabrication imperfections to the graphene edges along with the effect of diffraction.

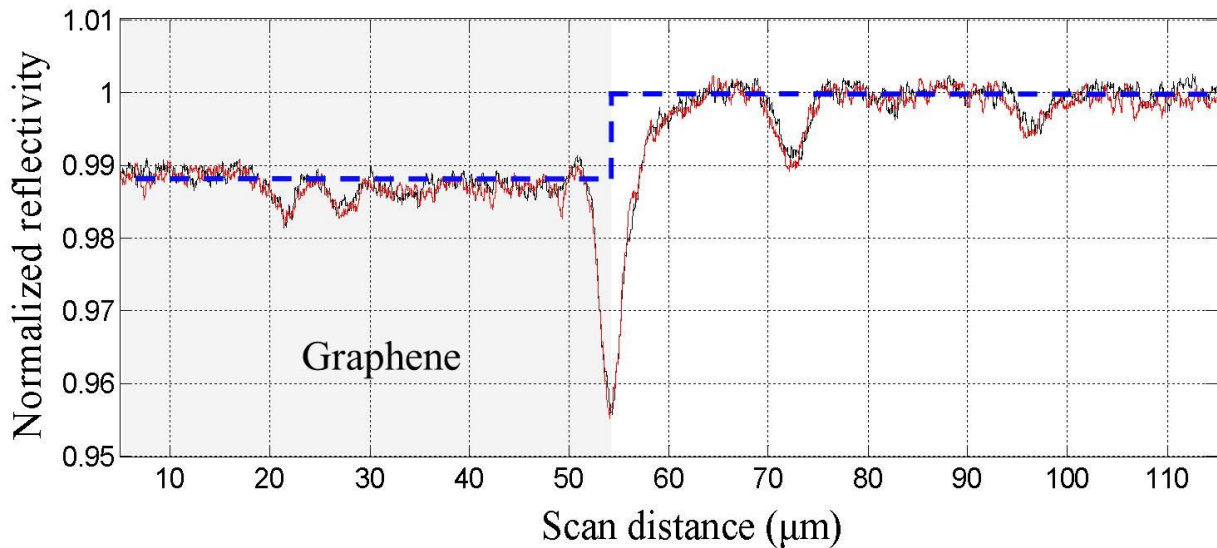


Figure: 2. 3. Normalized power reflectivity from sample surface measured with beam scanning across the edge of single-layer graphene in the forward (red) and backward (black) directions. No gate voltage is applied.

In order to measure the variation of optical power reflectivity R as the function of the applied gate voltage V , the position of the laser beam was fixed on the graphene. As this variation was expected to be less than 1%, the system had to be stable enough and the impact from laser power variation and interference caused by reflections from various optical components in the system had to be minimized. Thus, in this measurement, instead of using the mechanical chopper, a 5 kHz sinusoid voltage waveform with $2V_{pp}$ amplitude was directly applied on the graphene to synchronize the lock-in amplifier.

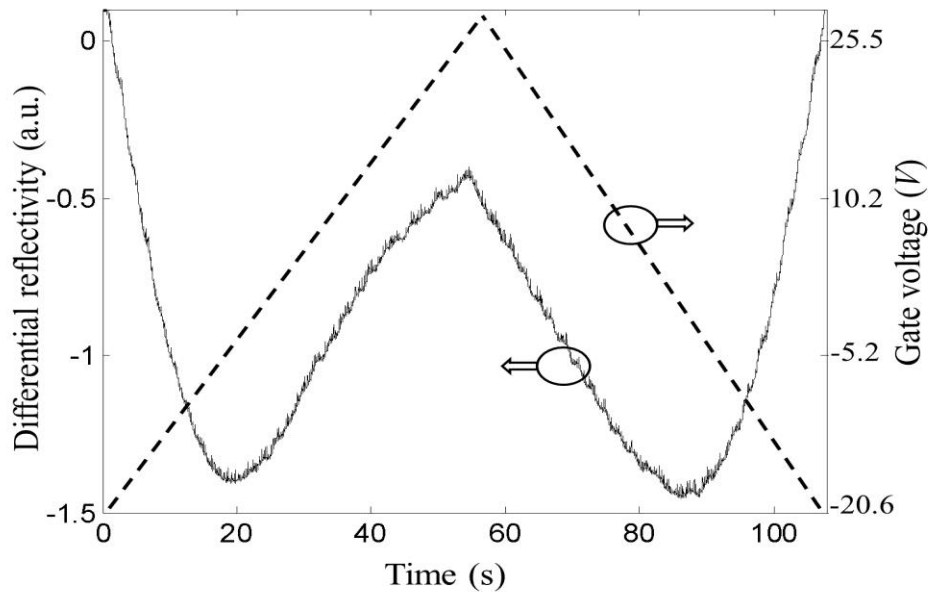


Figure: 2. 4. Measured differential reflectivity (continuous line) and the applied linear scan of gate voltage (dashed line) as the function of time.

An adjustable DC gate voltage was added to the small-signal modulating waveform through a bias-tee as illustrated in Fig. 2.2. This is equivalent to a small-signal modulation on chemical potential of the graphene, and therefore the lock-in amplifier actually measures the differential reflectivity $\delta R(V)/\delta V$. Fig. 2.4 shows the differential reflectivity measured on the graphene when

the DC bias voltage was linearly ramped up and down between -20.6 V and 28.6 V, and the rate of this voltage scan was approximately 1.1 V/s. The gate voltage-dependent differential reflectivity shown in Fig. 2.4 demonstrates the tunability of graphene complex reflectivity, which is clearly not a linear function of the applied gate voltage. The measured $\delta R(V)/\delta V$ characteristics also depend on optical interference of the multi-layered structure of SiO₂/Si substrate. Another observation of Fig. 2.4 is that $\delta R(V)/\delta V$ depends on the direction of voltage scan, and this hysteresis is attributed to the charge trapping and storage in graphene.

The normalized change of the power reflectivity on the sample surface without and with the graphene can be calculated based on the multilayer interference theory as [36],

$$\Delta R / R_0 = \pi \delta_g \cdot \text{Re} \left\{ \frac{(1 - n_g^2)(1 + r_0)^2}{r_0 \lambda} \right\} \quad (2.3)$$

where r_0 is the optical field reflectivity of the substrate without graphene, and λ is the wavelength. For the SiO₂/Si substrate, $r_0 = (r_{01}e^{j\beta_{ox}d_{ox}} + r_{12}e^{-j\beta_{ox}d_{ox}})/(e^{j\beta_1 d_1} + r_{01}r_{12}e^{-j\beta_{ox}d_{ox}})$ and $R_0 = |r_0|^2$, where $b_{ox} = 2\pi n_{ox}/\lambda$ is the propagation constant of the oxide layer, $r_{01} = (n_{ox} - 1)/(n_{ox} + 1)$ and $r_{12} = (n_s - n_{ox})/(n_s + n_{ox})$ are Fresnel reflectivities at air/SiO₂ and SiO₂/Si interfaces, respectively, with n_{ox} and n_s refractive indices of SiO₂ and Si. Fig. 2.5(a) shows the real and imaginary parts of the graphene refractive index as the function of chemical potential calculated from Eq.(2.1). The bottom horizontal axis of Fig. 2.5 indicates the applied gate voltage, which is related to the chemical potential through Eq. (2.2). We used $V_D=74$ V and $d_{ox}=95$ nm to obtain the best fit to the measured results. The solid line in Fig. 2.5(b) is the graphene induced power

reflectivity change calculated from Eq.(2.3), and the solid dot indicates $\Delta R/R_0 = 1.1\%$ at the gate voltage $V = 0$, as shown in Fig.2.

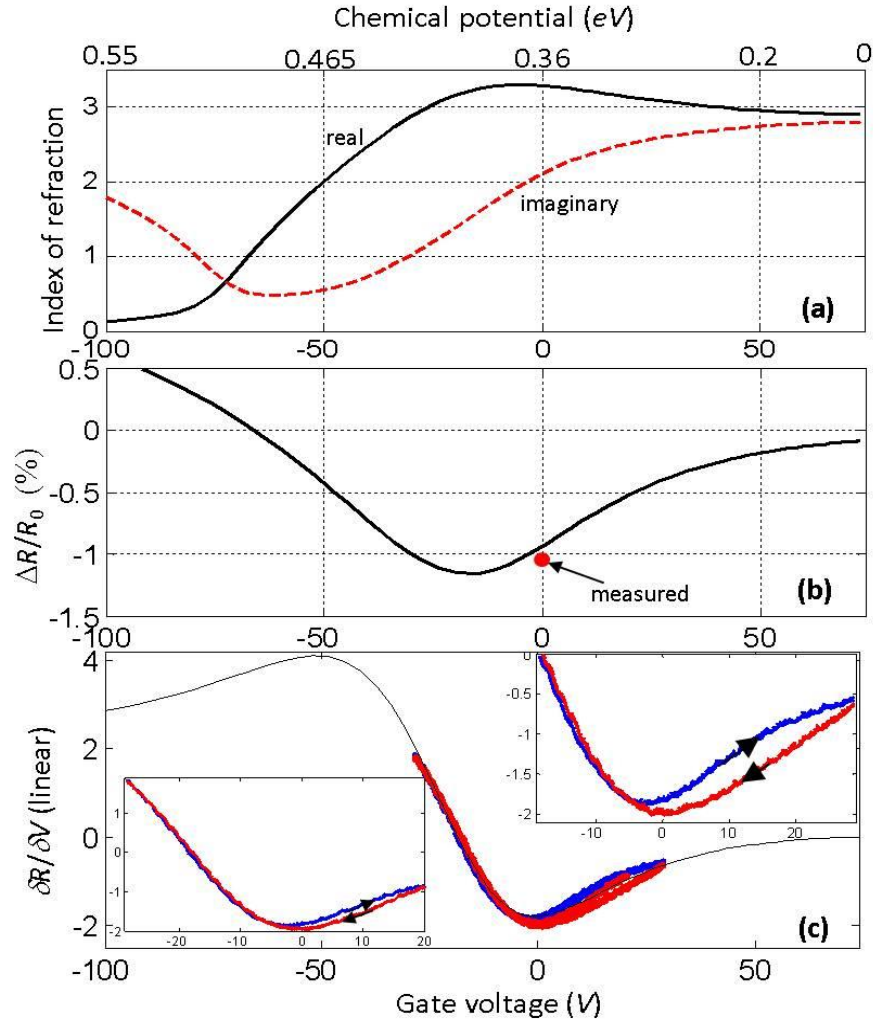


Figure: 2. 5. (a) Calculated complex index based on Kubo formula. (b) normalized power reflectivity change due to graphene layer on substrate (continuous line) and measured value extracted from Fig.4. (c) calculated (continuous line) and measured (dots) differential.

The continuous line in Fig. 2.5(c) shows the calculated differential reflectivity $\delta R(V)/\delta V$, which is the derivative of the solid line in Fig. 2.5(b). Dotted lines in Fig. 2.5(c) are $\delta R(V)/\delta V$

measured with linear scanning of the gate voltage V , and the results agree reasonably well with the calculated values, except for the apparent hysteresis in the measured curves that are not considered in the theoretical model. The insets in Fig. 2.5(c) show enlarged views of the measured differential reflectivity R for the gate voltage scan between -29 V and +20 V (bottom left), and between -20 V and +29 V (top right). Hysteresis is clearly shown in both of the two measurements, indicating different reflectivity changes corresponding to the ramp-up and ramp-down process of the applied voltage. The hysteresis loop is wider when the graphene is biased closer to the Dirac point. The characteristic of hysteresis has been previously reported in gate voltage dependent I_{SD} in graphene-based FET structures [48-49], but not for the optical properties such as the change of power reflectivity. This effect has to be considered in the design and application of graphene based photonic devices.

2.3. Indium Tin Oxide

Indium Tin oxide (ITO) is a composite material with the composition of indium, tin and oxygen in various proportions in transparent conduction oxide material group. By changing the proportions, it is possible to change the carrier concentration of ITO, which profoundly changes the plasma frequency given by eq.2.4.

$$\omega_p = \sqrt{\frac{Ne^2}{\epsilon_0 m^*}} \quad 2.4$$

where N is the carrier concentration, m^* is the effective mass of the electron, e is the charge of an electron and ϵ_0 is the free space permittivity.

From the basic Drude Model, permittivity of ITO can be written as

$$\varepsilon = \varepsilon_{\infty} - \frac{\omega_p^2}{\omega(\omega - i\gamma_p)} \quad (2.5)$$

where ε_{∞} is the permittivity at very high frequency, and ω_p and γ_p are plasma frequency and relaxation frequency respectively.

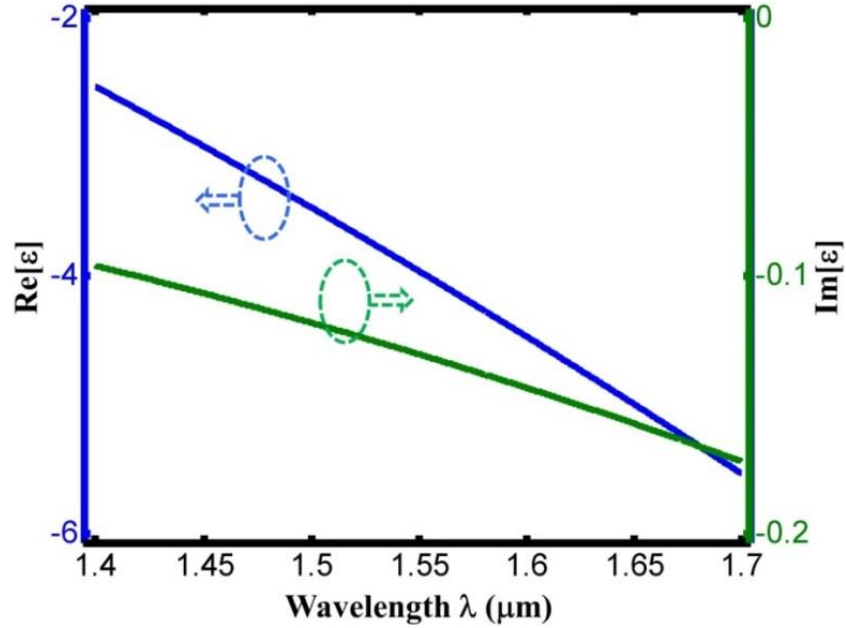


Figure: 2. 6. Permittivity of ITO w.r.t. wavelength in NIR regime

With very high doping concentration $N = 1.38 \times 10^{27} / \text{m}^3$, with modeling parameters $\varepsilon_{\infty} = 3.8$ and $\gamma_p = 0.0845 \text{ eV}$ [50], the real and imaginary part of the permittivity is shown in figure 2.6 over a broad wavelength in NIR region. Moreover, depending upon the chemical procedure and the proportion of the materials it is possible to achieve different dielectric properties of ITO. For a very thin layer of ITO, the free carrier concentration can be modified by applying external potential [51]. Using the modeling parameter $\varepsilon_{\infty} = 4.55$ and $\gamma_p = 724.6 \text{ THz}$, permittivity of the ITO is shown in figure 2.7 with different carrier concentration at 1550 nm. It is clear that; real

part of permittivity of ITO can be modified from positive to all the way to negative value which promises to a tunable material in the field of tunable photonic device.

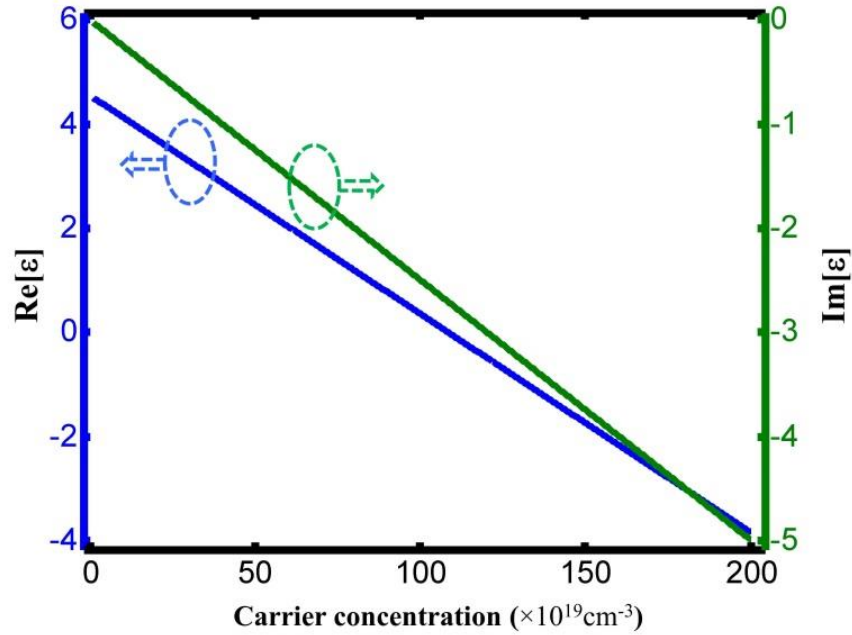


Figure: 2. 7. Permittivity of ITO for different carrier concentration in NIR regime

2.4. Vanadium di Oxide

The search for advanced photonic materials with high modulation efficiency and fast response time has been a continuous challenge in the field of nanophotonics. Realization of functional photonic devices, such as optical modulators and switches that provide rapid and energy efficient optical response at compact size, relies heavily on the fundamental properties of materials [52-54]. Vanadium dioxide (VO_2) is a promising candidate for a variety of photonic and optoelectronic applications that encompass large, broad-spectrum and ultrafast optical responses while suitable for integration with silicon photonics when needed [55]. A distinctive property of VO_2 is the capability of reversible dielectric-metal phase transition (DMT) which occurs near a

critical temperature T_c in the vicinity of 67°C . This transition is associated with drastic changes in the refractive index and resistivity of the material [56-57]. DMT can be induced thermally [58], optically [59] and electrically [60], on an ultrashort timescales of less than 100fs [61]. Although the material properties of VO_2 have been studied extensively, argument on the exact mechanism behind phase transition still exists. Various applications utilizing its optically-induced refractive index modulation (Δn) have been reported, such as tunable resonators [46], filters and modulators [62-63], optical phase controllers [64], switches and photodetectors [65]. However, a major drawback of VO_2 is the relatively long recovery time of the transition back from the metal state to the dielectric state, which is usually longer than 10ns. This largely asymmetric response limits many potential high speed applications.

We present a systematic measurement, using a fiber-optic pump-probe setup in 1550nm optical communications wavelength window. We show that the optically-induced material phase transition in VO_2 is primarily related to the pulse energy. Although the refractive index change of VO_2 triggered by the pump pulse has a long recovery time, the induced optical frequency change on the probe, which is proportional to the time derivative of the index change (dn/dt), has a time scale only determined by the leading edge of the pump pulse which can be shorter than 100fs. This allows for ultrafast optically induced modulations. In particular, we demonstrate the feasibility of converting a CW probe source into a pulsed waveform due to the effect of short pump pulses on the probe through cross-phase modulation in VO_2 followed by a frequency discriminator.

2.4.1. Experimental Setup and Results

Figure 2.8 illustrates the fiber-optic experimental setup used to measure the transmission of the VO₂ sample in the 1550nm optical communications wavelength window. Two tunable semiconductor lasers were used as the pump and the probe sources, and both of them were operating in the continuous wave (CW). The pump laser emitting at 1550nm was intensity-modulated through a fiber pigtailed LiNbO₃ electro-optic modulator to create width-tunable optical pulses ranging from 200ps to 10ns. The wavelength of the probe laser was 1530nm. The electrical waveform applied to the electro-optic modulator was generated by an arbitrary waveform generator (AWG) with a sampling rate of 25GS/s, and the analog bandwidth of the modulator is 10GHz. After intensity modulation, the pump optical pulse train was amplified by two erbium-doped fiber amplifiers (EDFA), with a bandpass optical filter (1nm bandwidth) sitting in between them to minimize the saturation effect due to amplified spontaneous emission (ASE) on the 2nd EDFA. The pump and probe were combined through a fiber-optic wavelength division multiplexing (WDM) coupler and focused onto the pre-heated VO₂ sample through free-space. Transmitted light through the sample was collected using a 10X objective and coupled into the single-mode fiber pigtail of a second WDM coupler, which operated as a demultiplexer to reject the pump wavelength, allowing only the probe wavelength to reach the photodetector with a 12GHz electrical bandwidth. The detected electrical waveform of the probe was amplified and recorded by a real-time digital scope with 50GS/s sampling rate which was triggered by the AWG. The VO₂ sample temperature was set at approximately 58°C by a temperature controller, which is in the vicinity of the phase transition temperature of VO₂ [56], and was chosen to maximize the impact of pump pulse on the transmission reduction of the probe. The measurement was performed with 500 kHz pump pulse repetition rate with the width of the

pump pulse being varied from 200ps to 10ns. The peak optical power of the pump was fixed at approximately 5W, which was primarily limited by the EDFA saturation and stimulated Brillouin scattering (SBS) of the single-mode fiber.

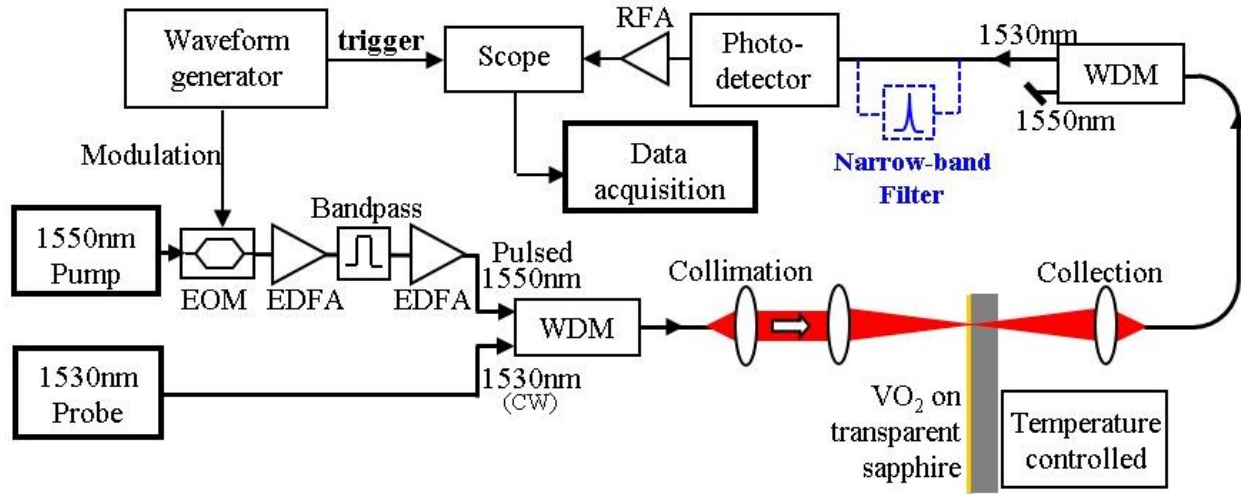


Figure: 2. 8. Experimental setup. WDM: Wavelength division multiplexer/demultiplexer between 1530nm and 1550nm. EOM: electro-optic modulator, EDFA: erbium-doped optical amplifier, RFA: radio frequency amplifier

As the VO_2 undergoes the phase transition from dielectric to metallic state, a dramatic change in its optical and electrical properties is anticipated, leading to an increase in the optical loss and a reduction of probe transmission. Figure 2 shows the measured probe absorption waveforms ($I-T$) at different widths of the pump pulse plotted in a logarithm scale (in dB), where T is the probe power transmissivity. These waveforms show that T is reduced instantaneously at the leading edge of the pump pulse due to an abrupt increase of the sample temperature. Previous studies have reported response times of less than 100fs for VO_2 phase transition upon fs pump excitation [61]. On the other hand the recovery time is much longer due to the slow heat dissipation after the pump pulse with the temperature reduction following a typical exponential decay process. Considering a constant pump peak power was used in this experiment, the pulse energy increases linearly with the pulse width, and the reduction in the probe transmission also increases

accordingly. Figure 2.9 also shows that the time constant of temperature decay gradually increases after the pump pulse because the reduction of temperature gradient near the focal point over time, which slows down the heat dissipation. This is shown as the slope reduction of the decay curves further away from the pump excitation event. Nevertheless, the decay rate of probe absorption immediately after the pump pulse is almost constant for all pump pulse widths from 0.2ns to 10ns shown as dashed straight lines, which is 37.5ns.

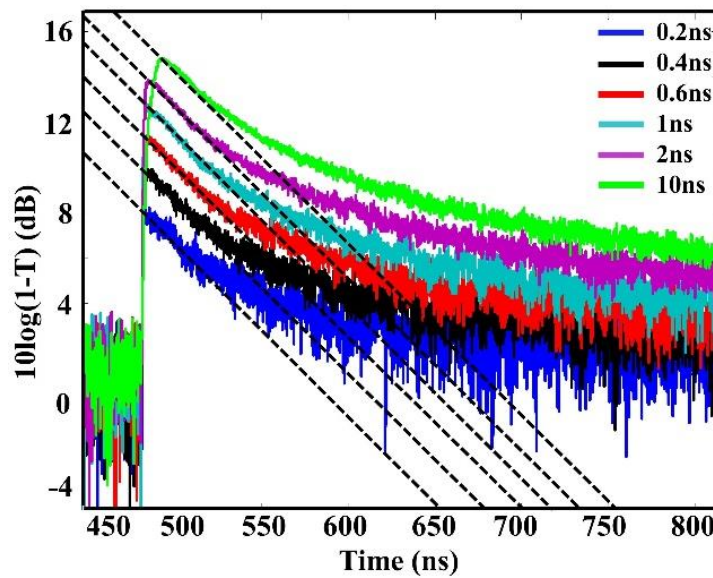


Figure: 2. 9. Measured waveforms of probe transmission T upon optical excitation of a 200nm VO₂ film via pump pulses of different time durations. Here (1-T) are plotted in logarithm scale to better demonstrate recovery time constants: The slopes of the dashed lines

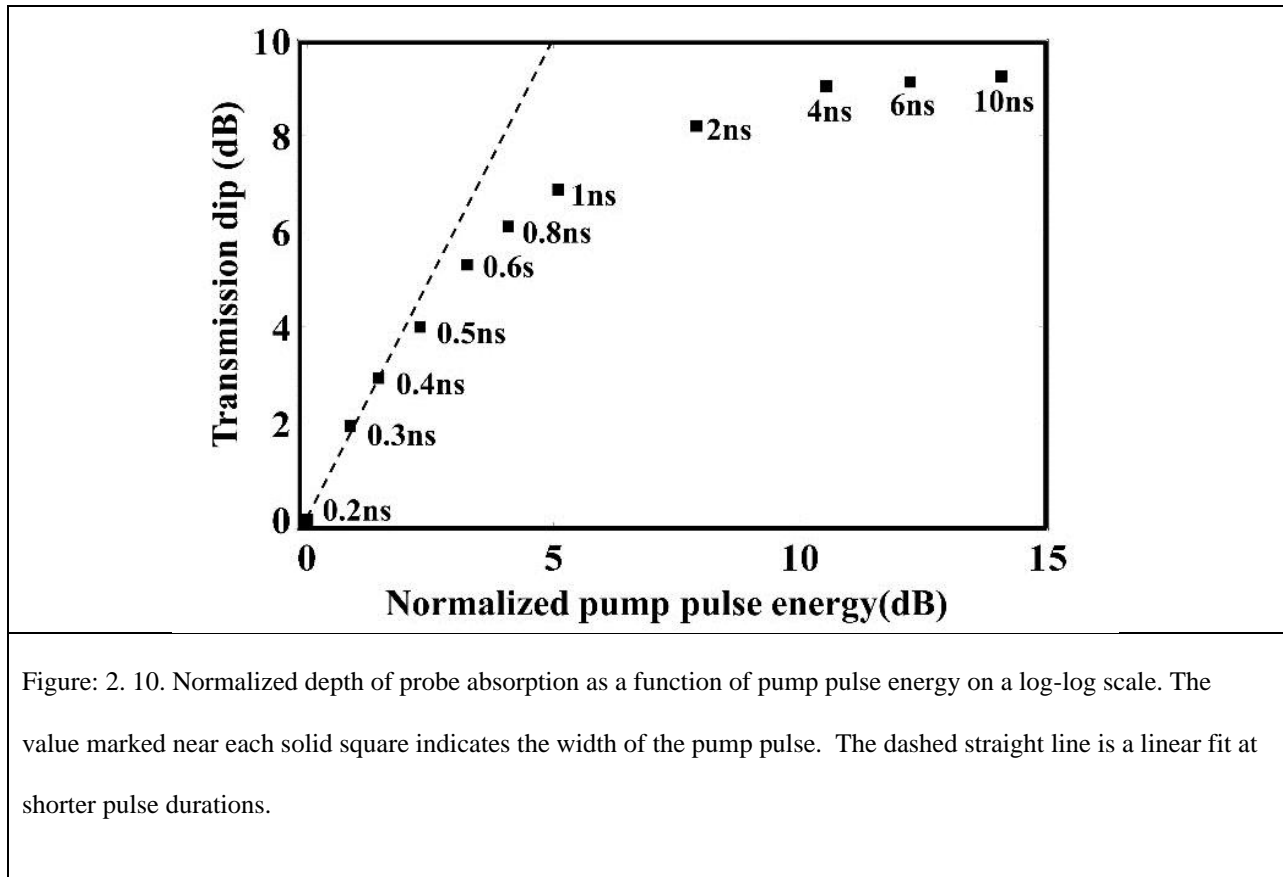
At a more fundamental level, it is important to understand the basic mechanism behind the optically-induced VO₂ phase transition, and clarify whether this transition is caused by the peak power, or by the energy of the optical pump pulse. To answer this question, a more systematic experiment was performed which measured the depth of probe absorption at pump pulses with different durations. In this case the pump peak power was kept constant so that the width change

is equivalent to varying the pulse energy. The results are shown in Figure 2.10 where solid squares are the normalized depth of probe absorption measured with pump pulses of different widths on a log-log plot. This figure indicates that when the pump pulse duration is much shorter than the phase recovery time of the VO₂ film, the depth of probe absorption is linearly proportional to the energy of the pump pulse. When the pump pulse is sufficiently long and no longer negligible in comparison to the phase recovery time constant (~37.5ns in this case), the efficiency of probe absorption starts to reduce. This is caused by the non-negligible thermal dissipation within the duration of the long pump pulses. Consequently, the sharpness of the phase change (from dielectric to metal) decreases accordingly. Therefore the probe absorption starts deviating from its initial rate, and tends to saturate with longer pump pulse durations. Note that in Figure 3 the linear fit at short pump pulse widths reveals approximately 2dB increase of probe absorption for a dB increase of the pump pulse energy. This super-linear characteristic is possible because the sample was pre-heated to the middle of its sharp phase transition region.

The optically-induced phase transition in VO₂ is associated with the change of the complex refractive index. It has been shown that the refractive index of VO₂ can be switched from $n_s = 3.243 + j0.346$ for the dielectric state to $n_m = 1.977 + j2.53$ for the metallic state [66]. The measurements of pump-induced probe absorption increase discussed so far in the literature were only related to the change of imaginary part of the refractive index. While the optical phase modulation on the probe relies on the pump-induced change related to the real part of the VO₂ refractive index. Considering the VO₂ film used in the experiment with a thickness $d = 200\text{nm}$, for a complete material phase transition from dielectric to the metallic state, the maximum optical phase change (dj) on the probe wave at $\lambda = 1530\text{nm}$ wavelength would be approximately:

$$\delta\phi = \frac{2\pi d}{\lambda} \text{Re}(n_m - n_s) \approx 1 \text{rad}$$

The time-domain response of this probe optical phase modulation $\delta\phi(t)$ is expected to have the same waveform as the probe absorption when the material phase transition is optically induced by a pump pulse.



The largely asymmetric response (shown in Figure2) with an ultrafast leading edge and a significantly slower falling edge, prohibits the generation of short optical pulses of the probe when passing through the VO₂ during its phase transition. However, the dynamic frequency modulation induced on the probe beam is proportional to the derivative of the optical phase modulation ($d\phi(t)/dt$). Thus, a large optical frequency modulation may be obtained

corresponding to the fast leading edge of the optical phase modulation, while the much slower falling edge would no longer contribute to this optical frequency modulation.

In our experiment with 10GHz electrical bandwidth of the electro-optic modulator, the rising time of the pump pulse was approximately 50ps. The leading edge of the optical phase modulation on the probe has the same time scale. The dynamic optical frequency shift of the probe can be estimated as:

$$\delta f = \frac{1}{2\pi} \frac{d\varphi(t)}{dt} = \frac{1}{2\pi} \frac{1}{5 \times 10^{-11}} = 3.2 \text{GHz}$$

However, due to the limited pulse peak power used in our experiments, the material phase change was limited to only a small fraction of the maximum phase transition between the dielectric and the metallic states of VO₂. Therefore the δf value calculated here only provides an upper limit, while the actual instantaneous frequency deviation of the probe obtained should be less than a GHz. The pump induced instantaneous optical frequency shift on the probe can be translated into an intensity modulation through a frequency-discriminator such as an optical filter. As shown in Figure1, this frequency modulation (FM) to intensity modulation (IM) conversion can be accomplished by adding a tunable fiber Fabry-Perot (FP) filter (shown in blue color in Figure1) before the photodetector. This FP filter has 100GHz free-spectral range and a finesse of 100, so that the width of the passband is approximately 1GHz, which is narrow enough to provide high FM/IM conversion efficiency for the probe signal with small FM modulation index. By setting the center of the FP passband to the static wavelength of the probe, an instantaneous frequency deviation of the probe would result in a reduced transmission through the FP filter, creating an intensity modulation which can be detected by the photodetector.

Figure 2.11(a) compares the measured probe waveforms without (top) and with (bottom) the FP filters before the photodetector. A sharp notch clearly appears in the waveform when the FP filter was applied for the FM-IM conversion.

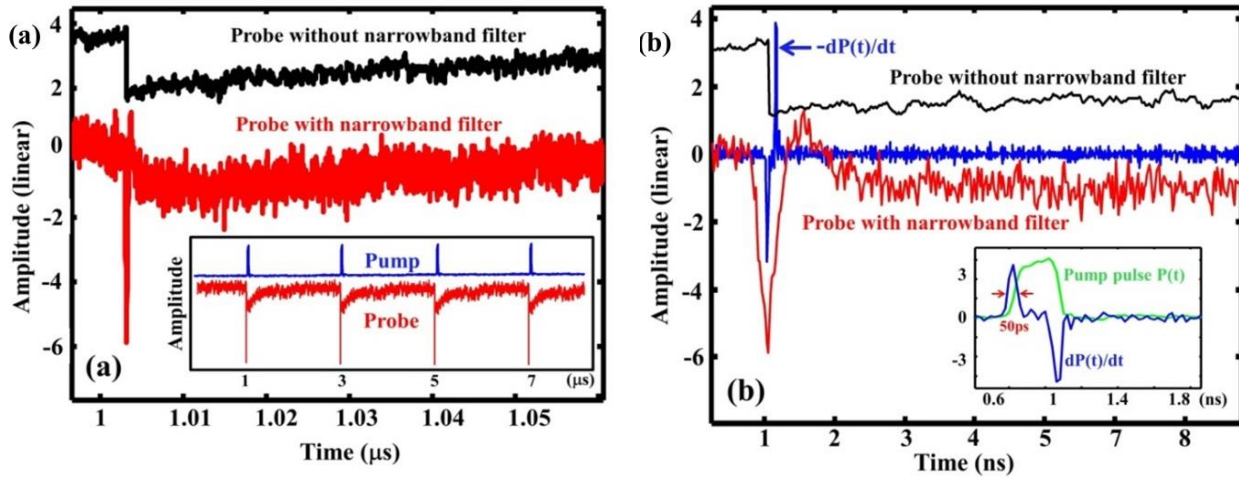


Figure: 2. 11. (a) Comparison of probe waveforms measured without (top) and with (bottom) the narrowband FP filter. Inset: pump and probe waveforms in a longer time span. (b) detailed view of probe waveform change in the transition region along with the inverse diff

Figure 2.11(b) reveals further details of the probe waveforms near the transitional region and the comparison with the inverse differential of the pump waveform ($-dP_{\text{pump}}(t)/dt$). The sharp notch in the FP filtered probe waveform corresponds to the leading edge of the pump pulse which instantaneously induces the phase transition in the VO_2 film. Whereas, the material phase transition after the falling edge of the pump pulse is too slow to induce any meaningful frequency deviation on the probe. The inset of Figure 4(b) shows the pump waveform $P(t)$ with 200ps pulse width together with its time derivative $dP(t)/dt$. This plot indicates that the differential of the pump pulse leading edge has a temporal width of approximately 50ps.

2.5. Conclusion

The reflectivity variation across the edge of CVD graphene on a SiO₂ (90 nm)/Si substrate was measured at 1550 nm optical communications wavelength. The measured change of reflectivity as the function of applied gate voltage agrees reasonably well with the theoretical prediction based on modeling using the Kubo formula. This verifies the tunability of complex refractive index of graphene, which is the most important parameter for the design of graphene based photonic devices for optical communications.

We have measured the phase transition of a 200 nm VO₂ film on a sapphire substrate at different pump pulse durations. The results show that the phase transition from dielectric to metallic state of VO₂ specifically depends on the energy of the excitation pump pulse, as long as the width of the pulse is much smaller than the phase recovery time from metallic back to the dielectric state. Moreover, during the leading edge of the pump pulse, a fast phase transition in the sample occurs and consequently an optical phase ($\delta\phi$) transient is introduced in the probe. We have shown that the derivative of this optical phase transient causes an instantaneous frequency shift of the probe. Therefore, by using a narrowband optical filter centralized at the probe wavelength, we were able to transform the optical FM into an IM and consequently generate short pulses at the probe wavelength with the same repetition rate as the pump. The width of the optical pulse generated in the probe is independent of the phase recovery time. However, the periodicity of the probe pulse waveform has to be longer than the phase recovery time of the VO₂.

Chapter III:

Photonic Devices

Functionality of photonic devices are resemble to the electronic devices. But, due to limitations of frequency dependent loss and high speed application of electronic devices, photonic devices are the parallel research universe with light wave so called scientifically known as the flow of photon. In last few decades, a drastic improvement on photonic devices together with plasmonic effect provide a new horizon to develop ultra-high speed, compact system with higher functionality per area.

3.1. Introduction

In a conventional ridge SOI waveguide, the interaction of modal electric field with Graphene is very low. Depending on the position of Graphene inside the waveguide, loss due to graphene varies over different chemical potential. Schematic diagram of ridge waveguide with a layer of graphene is shown in figure 3.1(a). Height and width of the waveguide are 300 nm and 420 nm respectively. Fundamental modal loss of the waveguide for 0 eV and 0.5 eV chemical potential of graphene are shown in figure 3.1(b) at different position inside the waveguide from top. It is prominent that the loss difference at 0eV and at 0.5 eV is maximum when graphene layer is at the middle of the waveguide. At middle position fundamental mode field is maximum, therefore interaction with graphene with modal electric field is also maximum.

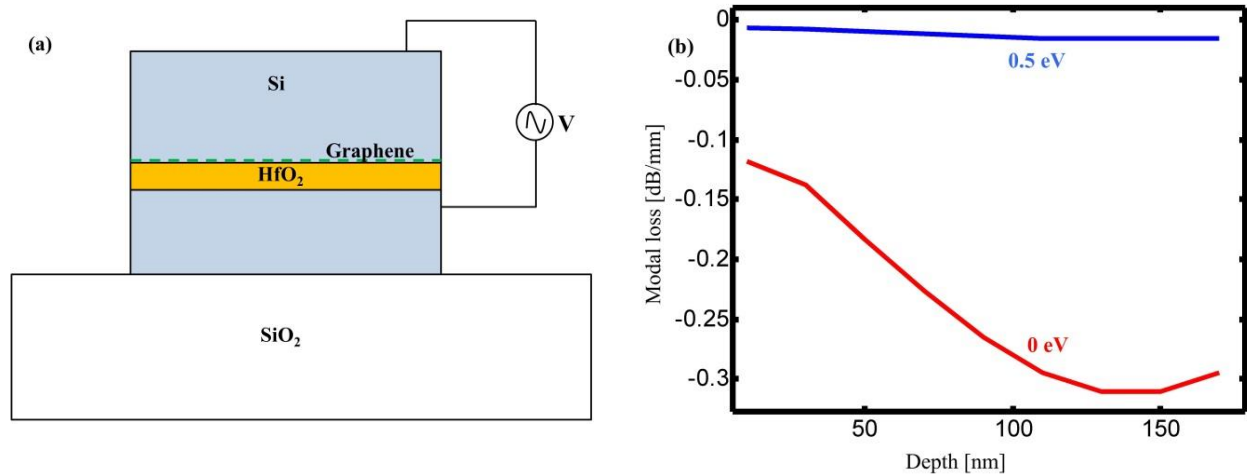


Figure: 3. 1. (a) Ridge waveguide with graphene and (b) fundamental mode loss at two different chemical potential.

Interaction with the graphene can be enhanced by plasmonic effect can be treated as tunable device which is discussed latter. μm^{-1}

Normally optical modulators are based on fundamental mode of the waveguide. With the help of electrically tuned optical absorption of indium tin oxide (ITO) in the optical communication wavelength regime, a novel approach to control both fundamental and 1st higher modes supported by the waveguide, is propose here. Reduction of size with simultaneous handling capacity of two modes enhance the functionality per area of photonic system

3.2. NIR EOM based on plasmonic graphene

Due to the exceptional optical and electronic properties, graphene has attracted a great deal of attention in the scientific and engineering communities [67]. The two-dimensional (2D) atomic structure of graphene leads to a low density of states (DOS) for electrons and holes, making the chemical potential particularly susceptible to the density of carriers. The large shift in the

chemical potential, that can be achieved by applying a gate electric field across the graphene layer, produces an extra charge accumulation in the energy bands and enhances both inter-band and intra-band electron transitions, allowing for efficient tuning of graphene's electric and optical properties. Such mechanisms have been successfully exploited for many practical applications, such as field effect transistors (FETs) [68-69], photodetectors [70-71], and electro-absorption optical modulators [72-73].

The graphene-based electro-optic modulator relies on the gate voltage-dependent optical absorption of graphene [72-73]. Although the absorption coefficient of graphene is extremely large compared with other materials commonly used in the near infrared (NIR) spectrum (3 orders of magnitude higher than that of germanium at 1.5 μm , and 4 orders of magnitude higher than that of silicon at 1 μm), the total absorption of a monolayer graphene is only about 2.3% for vertically incident light, simply because of the atomic thickness. Planar waveguide structures have been implemented to increase the interaction length between the guided-mode optical field and the graphene [70-71]. An electro-absorption optical modulator with 10dB extinction ratio was achieved with a 100 μm -long silicon waveguide imbedded with a monolayer graphene [72]. Because the mode field diameter of a silicon optical waveguide is approximately 4 orders of magnitude larger than the thickness of a monolayer graphene, the interaction between the optical field and the graphene is intrinsically weak. As a consequence, the modulator has to have long enough waveguide to achieve the required electro-optic tunability and the signal extinction ratio, which would result in relatively large capacitance, slow modulation speed and large electrical power consumption. Thus, enhancing the interaction of optical signals with graphene is critically important to realize practical electro-optic devices that rely on the tunability of graphene.

We propose a novel hybrid photonic–plasmonic platform for the realization of a graphene-based optical modulator operating at telecommunication wavelengths. Plasmonic structures represent an interesting avenue for the enhancement of light–matter interaction in graphene monolayers, mediated by the strong local optical field associated with surface plasmonic resonances [74]. In fact, plasmonic excitations in micro/nano-structured graphene have been explored in far-infrared (FIR) and THz spectral regions [75-77]. In the previously reported graphene-based NIR electro-absorption modulators, modulation is based on the tunable absorption of graphene, while in the present scheme; the graphene provides a mechanism of tuning on and off the resonant absorption of a plasmonic waveguide. As conventional noble metals such as Au and Ag have their plasma frequency in the visible or ultraviolet (UV) wavelengths, we have considered photonic waveguides loaded with indium tin oxide (ITO) nanostructures placed in close proximity of the graphene layer to maximize the sensitivity of the plasmonic resonance to the dielectric properties of graphene in the NIR region. In exploiting this mechanism, we have designed an ultra-compact graphene-based plasmonic electro absorption modulator that is able to achieve an order of magnitude reduction in the required waveguide length as compared to a graphene-based all-dielectric modulator.

3.2.1 Device configuration and operation principle

The configuration of the proposed electro-absorption modulator is schematically shown in Figure 3.2, which is based on a silicon ridge waveguide fabricated on a silicon-on-insulator (SOI) wafer. A monolayer graphene sandwiched in the middle of the waveguide provides the mechanism of electro-optic interaction through the modulation of its chemical potential. A 10 nm thick dielectric layer of HfO_2 is placed underneath the graphene to electrically isolate the top and the

bottom parts of the silicon waveguide. The width and height of the waveguide are 420 nm and 300 nm, respectively. To enhance the interaction between optical field and the graphene, a number of ITO bars are placed on top of the graphene layer to introduce the plasmonic effect. To simplify the analysis, the minimum separation between adjacent ITO bars was set as 10 nm which is longer than the decay length of plasmonic near-field, and the coupling of plasmonic modes between ITO bars can be negligible. In this configuration, the resonance condition of the plasmonic mode is susceptible to the dielectric constant of the surrounding materials including the graphene.

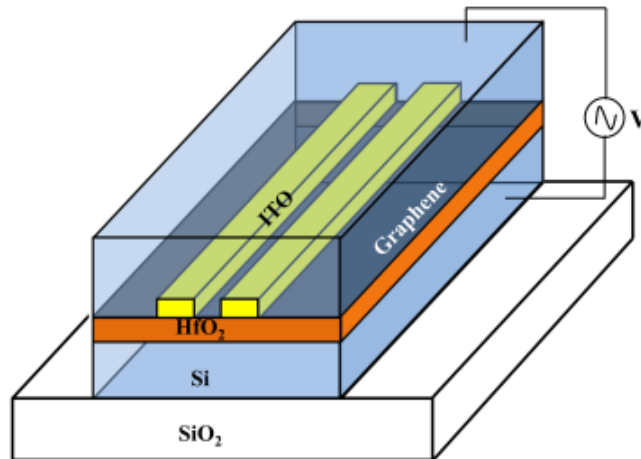


Figure: 3. 2. Schematic diagram of the hybrid plasmonic waveguide.

Electro-absorption modulator based on monolayer graphene imbedded in silicon ridge waveguide has been reported previously, with a maximum absorption efficiency of 0.1dB/ μm determined by the graphene in the waveguide [72], which was later increased to 0.16dB/ μm by using two separate layers of graphene in the waveguide [73]. The absorption efficiency of these modulators was primarily limited by the low interaction between the propagating mode of the waveguide and the atomic-thin graphene layer. In order to achieve a 20dB extinction ratio

typically required in telecommunications, the waveguide length has to be longer than 100 μm . The device capacitance, C_p , linearly proportional to the waveguide length, is a major limiting factor for practical applications, which causes slow modulation speed and high power consumption.

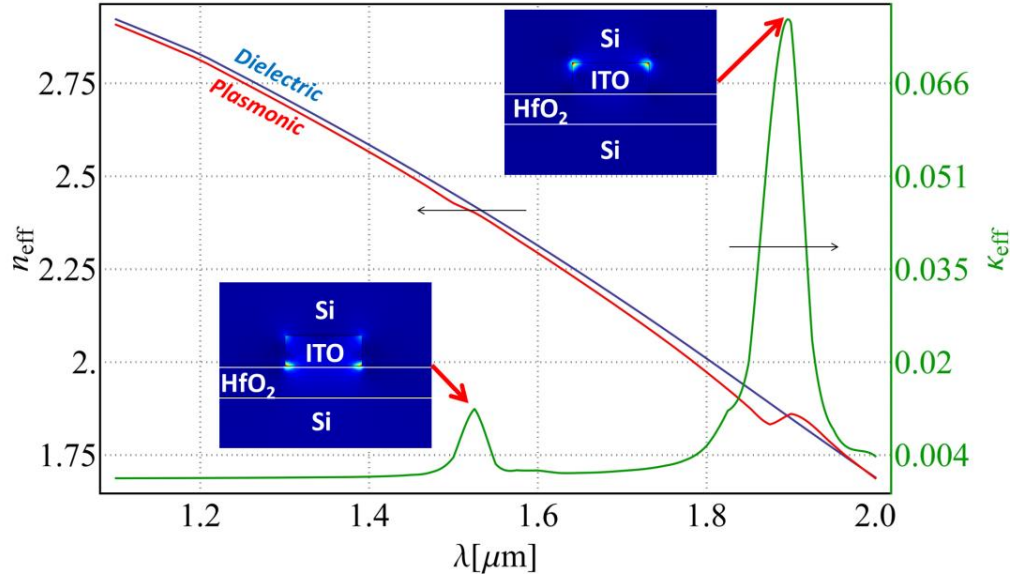


Figure: 3. 3. Waveguide dispersion curves for effective index and absorption coefficient with and without ITO bars. The insets show the norm of the electric field distribution around the ITO structure.

Surface plasmon resonances can be effective to confine the optical field far below the diffraction limit, and therefore to enhance the interaction between the optical field and the graphene placed in the plasmonic near-field region. The strength of plasmonic resonance is proportional to $1/(\epsilon_m + M\epsilon_b)$ where ϵ_m and ϵ_b are permittivities of the metal and the surrounding dielectric materials, respectively. M is a structural-dependent factor which varies with the geometry but is typically of the order of 1. Therefore the conditions for plasmonic resonance can be met when the metallic permittivity is nearly opposite to the permittivity of the surrounding medium. Although noble metals, such as Au and Ag, are commonly used to create surface plasmonic

effect, the negative values of their permittivities are very large and their plasmonic resonances are typically in the visible wavelengths [78-80]. In comparison, TCO has a much smaller permittivity (also negative), allowing for the plasmonic resonance to be in the NIR wavelength region, and the permittivity value can be adjusted by the change of carrier density through doping [81-82]. This permits precise tuning of resonance wavelength suitable for different dielectric constants of the surrounding materials. Therefore, the plasmonic effect introduced by the TCO bars shown in Fig.1 can help concentrate the NIR optical field into the monolayer graphene, and the efficiency of electro absorption can be significantly enhanced.

Figure 3.3 illustrates the effects of one ITO rod on the waveguide dispersion. The blue curve represents the effective index of the waveguide without the embedded ITO rod. The red curve represents the effective index of the waveguide when one embedded ITO rod rests on the HfO₂ layer. The effect of the ITO structure is to modify the effective index of the fundamental mode of the waveguide by providing a source of dielectric polarization. Notice that the effective index of the mode in the ITO loaded waveguide is almost uniformly lower than the index of the unperturbed dielectric waveguide, except for the spectral region near the second resonant peak around 1875nm. In any case the effective index of the mode never exceeds the index of the Si background medium. This is an indication that the ITO structure is operating on a localized transverse plasmonic resonance, without supporting a guided plasmon polariton along the waveguide. This interpretation is consistent with the field distributions shown in the insets of figure 3.3. In the spectral region near 1550nm the electric field of the surface plasmon is localized at the ITO-HfO₂ interface, consistent with the fact that the permittivity of the two media are nearly opposite at this wavelength. On the other hand, around 1875nm the electric field is mainly concentrated at the ITO-Si interface, again consistent with a condition of

localized surface plasmon resonance. It is important to point out that the fundamental mode field distribution is not significantly altered by the ITO rod, except for the enhanced field in proximity of the plasmonic structure. As a consequence of these mode-matching considerations, the reflection at the junction with a simple Si input guide of similar cross-section are expected to be negligible.

3.2.2 Results and discussion

Figure 3.4 shows the comparison of electric field intensity on the graphene layer with and without the ITO bars. It is evident that optical field concentration on graphene is increased by approximately 2 orders of magnitude underneath the ITO bars because of the plasmonic effect. The simulations were performed with COMSOL multiphysics software package, and the following parameters were used in the simulation: $\epsilon_d = 4$ is the permittivity of HfO₂, and $\epsilon_m = -3.99 + j0.13$ is the permittivity of ITO at 1550nm wavelength, corresponding to a doping density of $1.37 \times 10^{27} m^{-3}$ [81]. The permittivity of silicon is $\epsilon_{si} = 12.3$, which is used as the dielectric medium to form the waveguide core. Because the dielectric materials surrounding the ITO bars, including HfO₂, silicon and graphene, have different permittivity values, their combined effect determines the plasmonic resonance wavelength. The complex dielectric constant of graphene is a function of its chemical potential μ_c , and optical absorption can be turned from on to off when μ_c is switched from 0 to approximately 0.5eV, as shown in Figure 2.1. This not only allows the electric control of optical absorption but also provides an effective mechanism of switching on-and-off the plasmonic resonance when ITO bars are used.

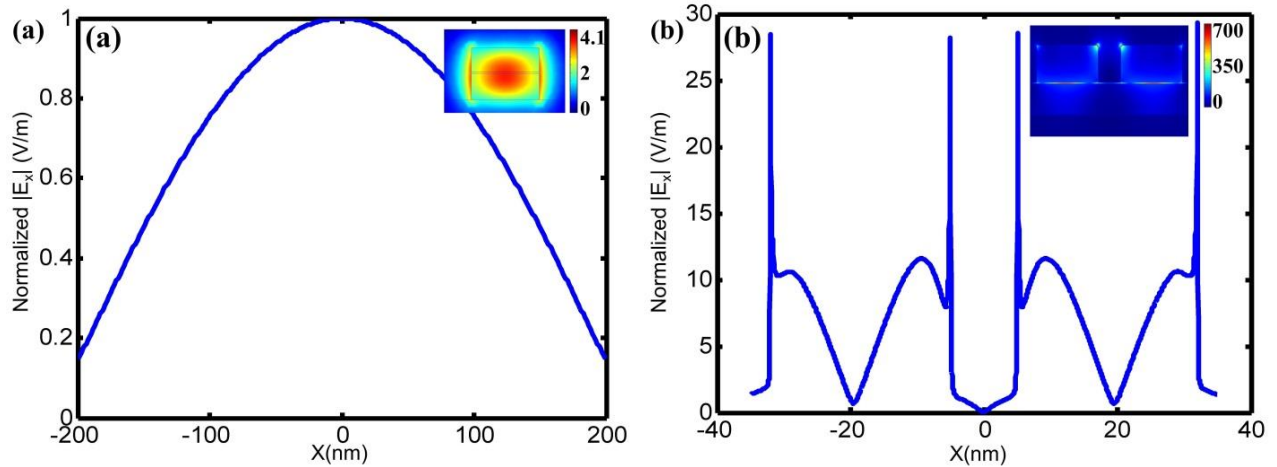


Figure: 3. 4. Normalized Electrical field $|E_x|$ distributions on the graphene layer of a graphene embedded SOI ridge waveguide without (a) and with (b) two ITO bars on the graphene.

To maximize the differential absorption of the NIR optical signal introduced by electrical gating, the cross-section geometry of ITO bars can be varied for optimization. Figure.3.5 shows the calculated optical absorption per unit length along the waveguide by varying the width (Figure.3.5(a)) and height (Figure.3.5(b)) of the ITO bar cross section. This was calculated with a single ITO bar placed on graphene layer in the middle of the waveguide. The absorption corresponding to 0 eV and 0.5 eV of graphene chemical potential shown in Figure 3.5 represent the minimum and the maximum loss values, and their difference indicates the extinction (on/off) ratio the modulator can provide. Figure.3.5 shows that the extinction ratio can be maximized by optimizing the geometry of the ITO bar cross-section, which indicates that tuning of plasmonic resonance condition through graphene chemical potential is the dominant mechanism in this plasmonic-graphene guided mode structure. This is fundamentally different from the graphene-based modulators previously reported [72-73], where electro-optic absorption of the graphene itself was the dominant mechanism, and thus the value of absorption per unit waveguide length

was intrinsically low. In the example shown in Figure 3.5, the optimum width and height of the ITO bar are in the vicinity of 27 nm and 12 nm, respectively.

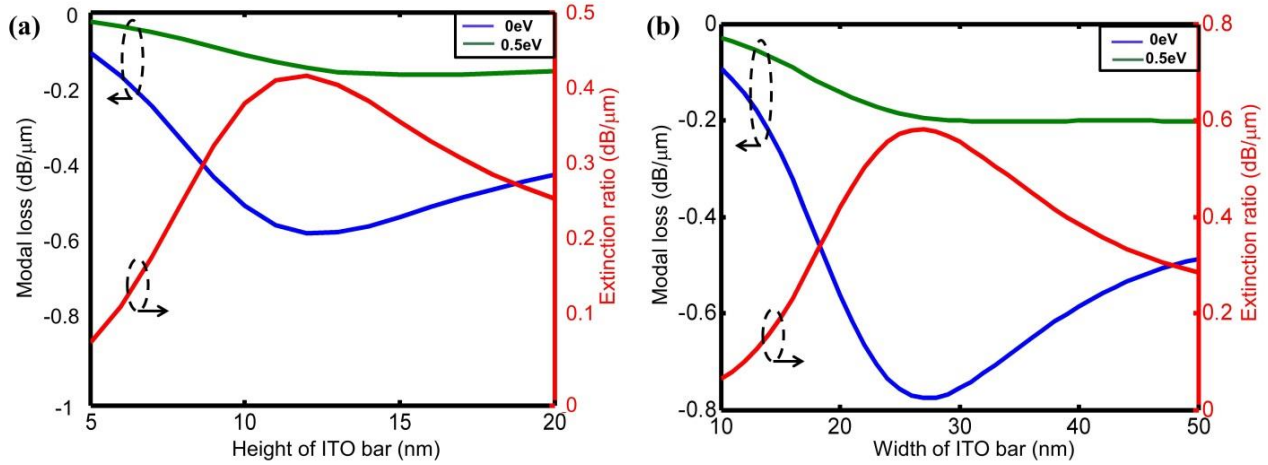


Figure: 3. 5. (a) Modal loss and extinction ratio for different height of the ITO bar with a fixed 20nm width. (b) Modal loss and extinction ratio for different width of the ITO bar with a fixed 12nm height.

As the width of the graphene layer in the silicon waveguide is 400nm, multiple parallel ITO bars can be used to further enhance the efficiency of controllable absorption. Figure 3.6 show the calculated unit-length attenuation of the plasmon mode as the function of the graphene chemical potential for different numbers of ITO bars separated by 10nm between each other. By increasing the number of ITO bars, the maximum differential absorption increases almost linearly because the 10nm separation between them is much longer than the spreading of the plasmonic near field, and thus interaction between plasmon modes of different ITO bars is negligible. Although up to 10 ITO bars can be accommodated over the 400nm wide graphene layer, a large number of ITO bars not only increases the extinction ratio, but also increases the minimum loss of the modulator, so that a trade-off has to be made for practical applications. For example for a modulator using 6 ITO bars, the extinction ratio reaches to approximately 5dB/μm

which is more than an order of magnitude higher than that without the plasmonic effect. According to figure 5b the configuration with 6 ITO bars also suffers from an insertion loss of about 1.7dB/ μm , which is a disadvantage common for optical circuits involving plasmonic effect. A tradeoff has to be made between the extinction ratio and the insertion loss when choosing the waveguide length. Nevertheless, the combination of plasmonic elements with a graphene layer allows significant reduction of the waveguide length, and the size of the electrode, which is essential to reduce the intrinsic capacitance of the device for high speed operation with low power consumption.

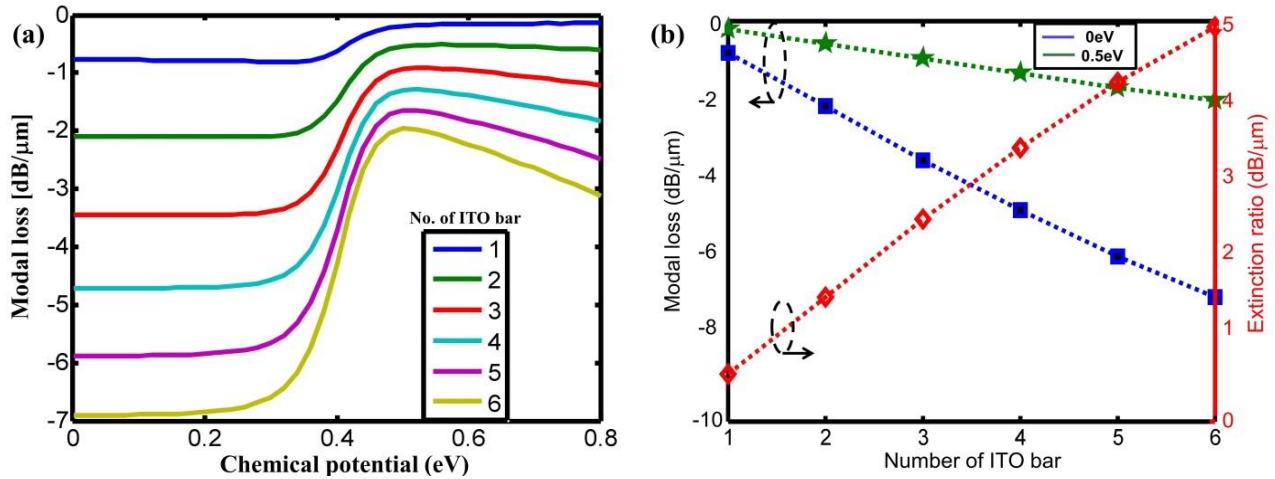


Figure: 3. 6. (a) Modal loss per μm as the function of graphene chemical potential for the waveguide with different number of ITO bars, and (b) Modal loss at 0 and 0.5eV graphene chemical potential for different number of ITO bars, and the corresponding extinction ratio.

Practically, the deposition of materials on graphene is difficult with many conventional physical or chemical vapor depositions as energetic particles and reactive chemicals from the deposition sources cause damages on graphene. This problem may be solved by evaporating a thin protecting interfacial layer such as Al film on graphene and converting it to insulating Al_2O_3

upon exposure to oxygen before ITO and Si layers growth atop using atomic layer deposition. [82-84]

3.3. Mode-multiplexed modulator

Following the success of CMOS electronics, the proliferation of photonic technology relies on the ability of large scale integration to drastically enhance the functionality, lower the per-device cost, and improve the reliability of integrated optical components. As already highlighted in the 2005 International Technology Roadmap for Semiconductors (ITRS) [85], optical interconnects hold promise to meet the ever-increasing requirements of modern telecommunications and processing systems in terms of speed and power consumption. Nanophotonic systems [86] in particular are emerging as one of the most promising technologies for on-chip dense photonic/electronic integration. In fact, scaling down the size of photonic components, compatibly with the constraints imposed by the physics of electromagnetic propagation, can simultaneously increase the bandwidth of operation, decrease the power consumption, and increase functionality-per-area (FPA).

During the past decade several photonic-modulator architectures have been developed. Silicon-based structures are attractive from a technological point of view, however, due to the weak electro-optic coefficient of silicon, electro-optic modulators relying on silicon alone [9] require large device footprints on the order of millimeters. The use of high-Q ring resonator structures [10-11] has been shown to partially circumvent this problem, allowing for the reduction of devices footprint to micron-size dimensions but at the expense of the reduced device bandwidth. Other CMOS compatible architectures featuring materials with superior electro-optic properties

have been extensively studied. In particular, graphene-based electro-absorption modulators have been demonstrated [72, 87], and plasmonically-enhanced graphene-based modulators have been proposed [88-90] to improve the performance of such devices. Transparent conductive oxides (TCO) such as indium-tin-oxide (ITO) and aluminum-zinc-oxide (AZO) have recently emerged as promising candidates for both plasmonic [50] and active photonic applications [51, 91]. The wide index-tunability of ITO by doping and by carrier-injection opens the possibility of actively switching between dielectric and plasmonic regimes, thereby enabling the efficient control of optical transmission. At the transition between such regimes – dielectric and plasmonic – lies the epsilon-near-zero condition (ENZ), which could offer significant improvements in the operation of electro-absorption modulators [32].

While materials research has opened new avenues in nanophotonics, many aspects related to electromagnetic design are still to be investigated and fully exploited. Here we consider the problem of increasing FPA from an electromagnetic standpoint and propose novel design principles for nanophotonic modulators that take advantage of modal degrees of freedom in order to effectively double the modulation bandwidth of such devices by introducing additional electromagnetically orthogonal channels that can be modulated independently.

In order to selectively modify the propagation properties – i.e. modal absorption and/or modal index – of different waveguide modes, two different modal characteristics may be used: modal polarization orthogonality, and reduced modal overlap. In order to employ modal polarization for selective modal modulation, a form of tunable polarization dichroism must be introduced in the waveguide core. Let us consider a waveguide described by a permittivity profile $\varepsilon_w(x, y)$ supporting two modes: “mode 1” with fields $\mathbf{E}_1, \mathbf{H}_1$, and “mode 2” with fields $\mathbf{E}_2, \mathbf{H}_2$. Let us also

assume that a thin conductive surface with surface conductivity $\bar{\sigma}_2$ is inserted in the waveguide cross-section so as to be perpendicular to electric field lines of mode 1 at every point. Under these conditions such conductive surface would only attenuate mode 2, while leaving mode 1 unaffected. Formally one may write the perturbed permittivity distribution of the waveguide as:

$$\epsilon_0 \bar{\epsilon}(x, y) = \epsilon_0 \epsilon_w(x, y) + i \frac{\delta[s_2(x, y)]}{\omega} \bar{\sigma}_2 \quad (3.1)$$

In equation (3.1) the argument of the Dirac's delta function is the implicit-form equation (i.e. $s_2(x, y) = 0$) of the conductive surface with unit normal $\hat{\mathbf{n}}_1 \parallel \mathbf{E}_1$. The surface conductivity tensor is at every point isotropic with respect to the local tangent plane to the surface s_2 , and it is null in the perpendicular direction.

Before deriving the modal losses, a word of caution is in order concerning the effects of the conductive surface s_2 on the modal field distribution. Such modification of the waveguide's layout in fact changes the electromagnetic boundary conditions, and therefore the modal field distributions $\mathbf{E}_1, \mathbf{H}_1$ and $\mathbf{E}_2, \mathbf{H}_2$ would be altered. Nevertheless if the conductive surface constitutes a small perturbation of the original structure, a perturbation expansion to the first order reveals that only the modal index is affected, while the modal fields are subject only to a second order correction [15]. Under such assumption, the dissipated power per unit length for mode 2 follows from Poynting's theorem, along with the orthogonality relation between modes, and the properties of the tensor $\bar{\sigma}_2$:

$$\frac{\partial P}{\partial z} = - \iint [\bar{\sigma}_2 \cdot \mathbf{E}_2] \cdot \mathbf{E}_2^* dx dy \quad (3.2)$$

Equation (3.2) indicates that mode 2 only experiences attenuation. A similar approach clearly could be adopted to selectively attenuate mode 1, by introducing a thin conductive surface perpendicular to the modal field \mathbf{E}_2 . Tunability of the aforementioned surface conductivity is necessary in order to realize a mode-multiplexed modulator exploiting the polarization-based modal dichroism just described. Graphene, already used in a number of modulator architectures [29,42,44,73,87-90,92], would offer ideal characteristics for the realization of the polarization-based mode-multiplexed modulators.

Reduced modal overlap can be exploited to generate “modal dichroism” by introducing a spatially localized absorption mechanism in regions in which only one specific mode concentrates most of its energy, while other modes have small (or ideally zero) amplitude. Notice that such conditions in non-magnetic media can be in principle met for purely transverse electric (TE) modes, but not for transverse magnetic (TM) or for hybrid modes, due to the presence of longitudinal components of electric field. Considering again a waveguide described by a permittivity profile $\varepsilon_w(x, y)$, a loss mechanism can be induced by perturbing the permittivity distribution as follows:

$$\varepsilon_0 \varepsilon(x, y) = \varepsilon_0 \varepsilon_w(x, y) + \frac{i}{\omega} [a_1 \sigma_1(x, y) + a_2 \sigma_2(x, y)] \quad (3.3)$$

Let us assume that the parameters a_1 and a_2 in the imaginary part of the perturbed permittivity profile (3.3) can be externally modified to assume values between 0 and 1. The power attenuation induced on two waveguide modes \mathbf{E}_1 and \mathbf{E}_2 can be written as:

$$\frac{\partial P_1}{\partial z} = -a_1 \iint \sigma_1(x, y) \mathbf{E}_1 \cdot \mathbf{E}_1^* dx dy - a_2 \iint \sigma_2(x, y) \mathbf{E}_1 \cdot \mathbf{E}_1^* dx dy \quad (3.4)$$

$$\frac{\partial P_2}{\partial z} = -a_1 \iint \sigma_1(x, y) \mathbf{E}_2 \cdot \mathbf{E}_2^* dx dy - a_2 \iint \sigma_2(x, y) \mathbf{E}_2 \cdot \mathbf{E}_2^* dx dy \quad (3.5)$$

In order to produce effective modal dichroism the conductivity profiles σ_1 and σ_2 must be chosen so as to minimize the cross-terms, i.e. the second term on the right-hand side of equation (3.4) and the first term on the right-hand side of equation (3.5). Notice that in general such terms, which are responsible for modulation cross-talk, are always greater than zero, as the argument of the integrals is definite positive. Nevertheless a proper selection of the waveguide modes can greatly facilitate the cross-talk minimization process.

As a simple heuristic guideline for the optimization of the conductivity profiles, the waveguide modes should be selected to have similar order and different symmetry with respect to at least one of the symmetry planes of the waveguide cross-section, as for instance in the case of the E_{11}^y and E_{21}^y modes of a rectangular waveguide [22] in which case the zeros of one mode tend to coincide with the maxima of the other and vice-versa. An additional benefit of such modal choice in terms of minimizing cross-talk is that if the conductivity profiles do not alter the symmetry of the waveguide permittivity distribution $\varepsilon_w(x, y)$, the power exchange between modes of different symmetry is zero. This is the strategy that we adopted in the design of the mode-multiplexed nanophotonic modulator discussed in the next section.

Here for the purpose of illustrating the concept of modal dichroism we consider a mode-multiplexed nanophotonic modulator based on a silicon-on-insulator (SOI) platform for electronic-photonic integration. The configuration of the proposed device is schematically shown in figure 1(a). The optical signal is carried by a multimode silicon ridge waveguide. The active components are three thin plates of ITO of thickness 10 nm that can be individually addressed by means of three gold contacts separated from the ITO structures by an insulating 20 nm layer of

SiO₂. The dimensions of the ridge waveguide are chosen to be 800 nm in width and 200 nm in height for operating at $\lambda = 1.55 \mu\text{m}$ wavelength.

3.3.1 Device configuration and operation principle

The physical mechanism of modulation in the proposed structure is the voltage-controlled free-carrier absorption in ITO. ITO is a degenerately doped semiconductor with free-carrier concentration that can be tuned by controlling the concentration of oxygen vacancies and interstitial metal dopants. In addition to doping, carrier concentration can also be electrically tuned. Near-unity index changes by carrier injection in ITO have been recently reported [29,51].

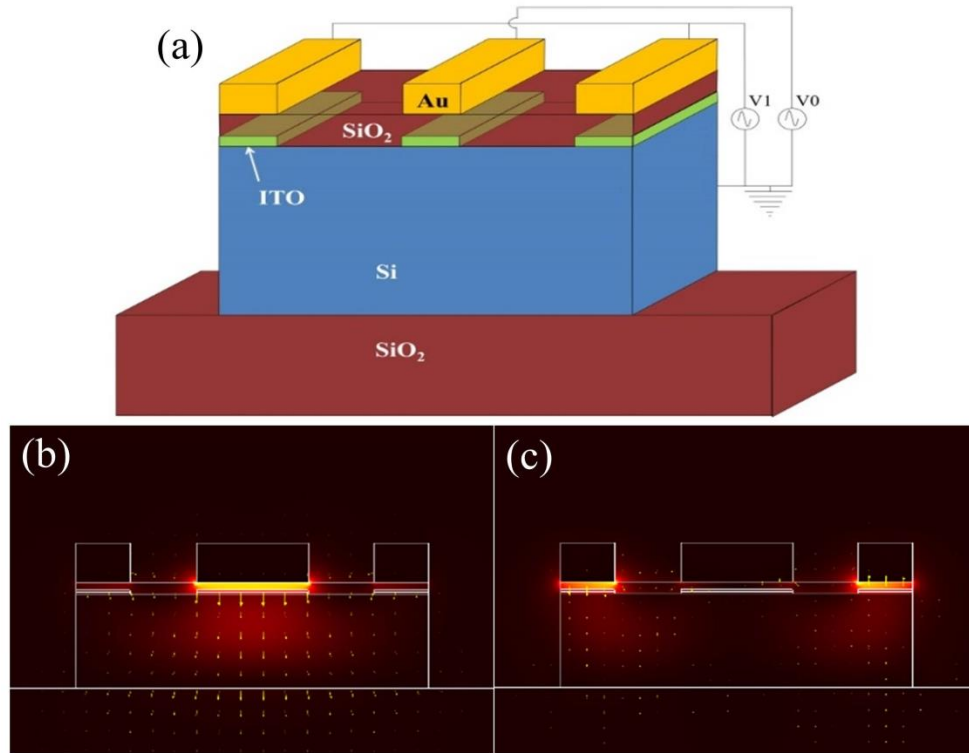


Figure 3.7. (a) Layout of the proposed mode-multiplexed nanophotonic modulator. (b) Electric field distribution of the E_{11}^y mode for $N_L=N_C=N_0$. (c) Electric field distribution of the E_{21}^y mode for $N_L=N_C=N_0$.

In the layout shown in figure 3.7 each of the ITO plates is arranged in a MOS capacitor configuration. With an applied DC potential, the static electric field produces a change in the free-carrier density inside the material by forming an accumulation layer at the ITO-SiO₂ interface. The carrier density in the accumulation layer, as obtained from the self-consistent solution of the Poisson's equation for a MOS capacitor is non-uniform, with a profile of the form [93] $n(z) = N_d \exp[\Phi(z)/\Phi_T]$, where N_d is the doping density in the ITO layer, $\Phi_T = k_b T/q$ is the thermal voltage and $\Phi(z)$ is the electric potential at position z within the accumulation layer, with $z=0$ coinciding with the ITO-SiO₂ interface. The depth of the accumulation layer is of the order of $d_{acc} \sim \pi L_D / \sqrt{2}$, where $L_D = \sqrt{\epsilon_0 \epsilon_{ITO} \Phi_T / (q N_d)}$ is the Debye length in the ITO layer [93].

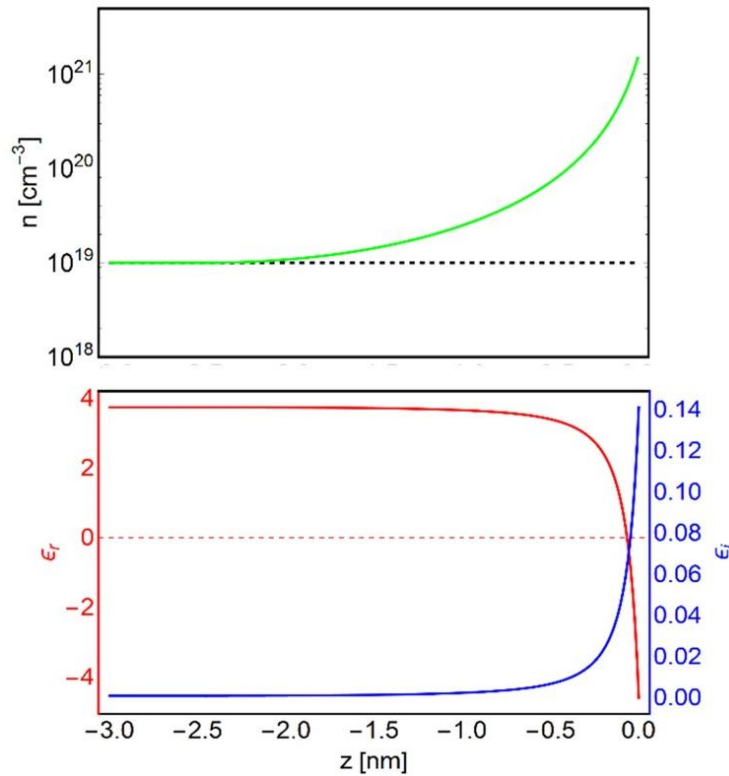


Figure 3.8. Carrier density (top), and real (red) and imaginary (blue) part of permittivity at $\lambda=1550\text{nm}$ in the accumulation layer of an ITO layer with doping concentration $N_d=10^{19}\text{cm}^{-3}$ under an applied voltage of 16.4V.

For our modulator we have considered ITO layers with a doping concentration $N_d = 10^{19} \text{ cm}^{-3}$. In the top panel of figure 3.8 we show the calculated carrier density in the accumulation layer for an applied voltage of $V = 16.4 \text{ V}$ across the 20nm SiO_2 spacer between the top gold electrodes and the ITO plates. For this voltage value the electric field in the SiO_2 spacer is 8.13MV/cm, which is below the breakdown value of $\sim 10 \text{ MV/cm}$ for this material. The corresponding real and imaginary parts of the ITO permittivity at $\lambda = 1550 \text{ nm}$ [50] in the accumulation layer are shown in the bottom panel of figure 3.8. At said wavelength and doping concentration, based on the Drude model parameters from Naik *et al.* [50], the ITO permittivity within the 2.5nm thickness of the accumulation layer varies from the background value of $3.74 + i0.00095$ to a value of $-4.59 + i0.14$ at the ITO- SiO_2 interface.

3.3.2 Results and discussion

Considering the mode profiles of the waveguide, we are only interested in y-polarization of the fundamental mode (E_{11}) and the 1st higher order mode (E_{21}). Cross-sectional view of the mode profiles are shown in figure 3.8(a). As shown in figure 3.8(b) the maximum intensity of electric field of E_{11} mode is at the middle of the waveguide, therefore the interaction with ITO plate at central position will be stronger than the end two ITO plates. Analogously, for E_{21} mode, where the maximum field intensity is away from the middle position of waveguide, electric field interaction with the end two ITO plates will be more than the middle ITO plate. Therefore, modulation of E_{11} can be done independently by modulating the voltage V_0 and E_{21} mode can be modulated by modulating the voltage V_1 between silicon waveguide and two extreme gold electrodes as shown in figure 3.7. Manipulation of V_0 and V_1 in such a way that the carrier concentration inside ITO bars varies in two stages of $1 \times 10^{19} \text{ cm}^{-3}$ and $8.6 \times 10^{20} \text{ cm}^{-3}$.

The permittivity profile shown in figure 3.8 has been used in the numerical modeling of the electromagnetic properties of the proposed modulator. The dimensions of the ITO plates have been optimized through parametric full-wave simulations [94] to maximize the modulation depth while maintaining a low cross-talk between modes, yielding a width of 200nm for the central ITO bar, and a width of 100nm for the lateral bars.

In figure 3.9 the effectiveness of the proposed modal dichroism mechanism is assessed by studying the modulator performance over the optical communication wavelength range from $\lambda = 1.5\mu m$ to $\lambda = 1.6\mu m$. The Drude model [50] along with the previously discussed MOS model for the carrier density profiles has been used to account for the frequency dependence of the permittivity of the ITO bars. Figure 3.9(a) shows the propagation losses experienced by the E_{11}^y under the various voltage bias configurations of the ITO bars. The green curve represents the case in which no voltage is applied to any of the ITO bars, and therefore is representative of the device insertion loss. The red curve shows the case in which a voltage $V = 16.4V$ is applied to the central ITO bar, while the lateral bars are left unbiased. In this situation the propagation loss of the E_{11}^y raises to about $0.9dB/\mu m$. Finally the blue curve represents the complementary case of a voltage $V = 16.4V$ applied to the lateral bars, while leaving the central bar unbiased: as desired only a marginal increase in the propagation loss of the E_{11}^y mode is observed. The corresponding curves for mode E_{21}^y are presented in figure 3.9(b). As expected, the propagation loss for mode E_{21}^y is strongly affected by the conductive state of the lateral ITO bars, while it remains nearly unchanged by a bias applied to the central ITO bar. These simulations clearly confirm that the proposed structure displays modal dichroism and can be employed as a mode-multiplexed nanophotonic modulator. The proposed modulator shows performances in line with conventional

single-mode ITO modulators recently reported in the literature [32], while increasing the functionality per-area by offering the possibility independently modulating two modes.

The theoretical MOS model presented here and in e.g. [32] for the induced carrier density in the ITO plates appears to actually underestimate the performance of actual devices[91]. In fact experimental measurements on very similar structures [51, 91] have shown (especially in [91]) performances consistent with much higher carrier densities than the MOS model would predict for the corresponding applied voltages. While some justifications have been proposed [95], more sophisticated models of the accumulation layers in transparent conductive oxides should be explored. This is beyond the scope of this article, since the main focus of this work is to illustrate nanophotonic modal dichroism.

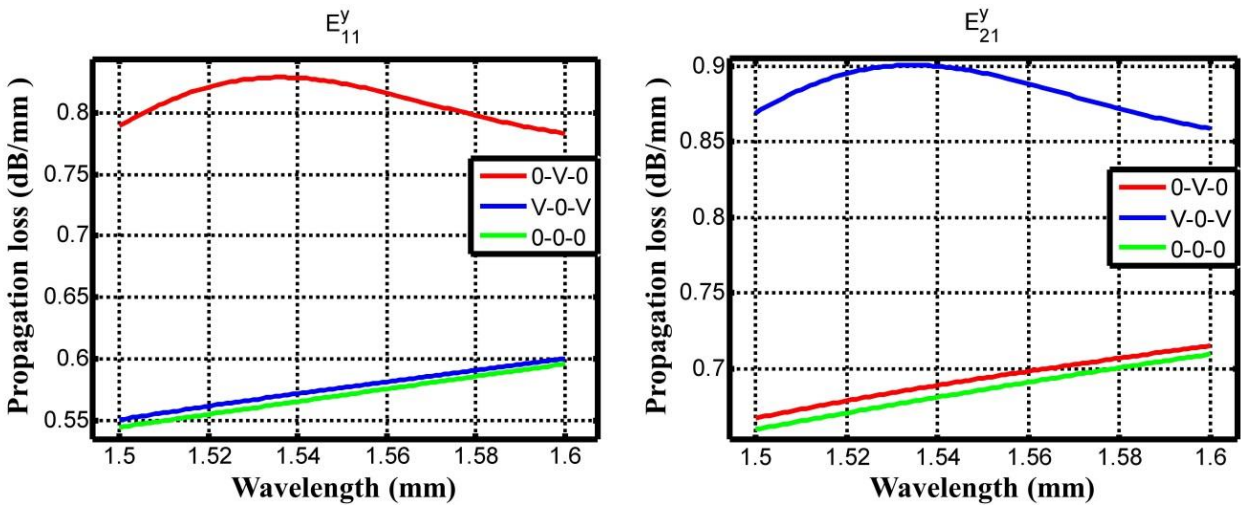


Figure 1.9. Propagation loss of the (a) E_{11}^y and (b) E_{21}^y modes under various electric bias configurations as indicated in the plot legends.

3.4. Metamaterial assisted tunable photonic coupler

The introduction of metamaterials (MM), Epsilon-Near-Zero (ENZ) materials and Surface Plasmon Polariton (SPP) has revolutionized photonic technology by offering unnatural behavior of electromagnetic waves and breaking through the barrier of diffraction limit in the design of integrated photonic circuits. Squeezing, tunneling, confining below diffraction limit, and bending of EM waves are the top most mysterious exciting properties of these new inclusions [96-98]. Various novel structures based on plasmonics effects have been proposed to redesign optical components such as filters, modulators, sensors etc. with considerable reduction of device size and higher efficiency have been investigated over past decade [99-101]. On top of that, single layer graphene with tunable surface conductivity provided an additional mechanism in the design of plasmonic circuits, which has been used to create integrated photonic devices such as modulators, beam splitters, antennas to operate in the near infrared region [88,102,103]. Among these, metamaterial, basically an artificially created material which has capability to provide hyperbolic dispersion relation, opens up a new era of optics [104-107, 109-110]. The metamaterial composed of periodic graphene and dielectric layers can provide a highly efficient tunable hyperbolic medium, ideal for electro-optic device applications [44].

For integrated photonic devices, functionality per area (EPA) is a basic figure-of-merit. Nanophotonic system in particular is emerging as one of the most promising technologies for high density photonic-electronic integration. Utilizing the physics of electromagnetic propagation in ENZ material for the design of photonic devices can increase the bandwidth of operation, decrease the power consumption and increase the FPA [108]. Directional coupler is a fundamental building block in optical circuits to combine, split and route optical signals. The ability of tuning optical coupling efficiency of a directional coupler through electronic control

can enable modulation and dynamic routing of optical signals which is essential for functional photonic integrated circuits.

Here we present an integrated silicon photonic directional coupler design based on uniaxial metamaterial or “crystal” composed of periodic single layer graphene and dielectric. This allows the tunability of the power coupling coefficient at 1550nm optical communication wavelength. Our theoretical analysis and numerical simulation indicate that this graphene based hyperbolic medium is able to provide efficient control of optical signal via externally applied voltage, which is an ideal bridge between optical and electronics domains. Additionally, due to the presence of high index anisotropic metamaterial the device size can be miniaturized to increase the functionality per area for integrated photonic applications.

3.4.1 Tunable Metamaterial

The unit cell of the MM used here is formed by two different materials of permittivity ε_1 and ε_2 with thickness d_1 and d_2 respectively as shown in figure 3.10. The periodicity of the array is denoted by $d \equiv d_1 + d_2$. For mathematical simplicity, individual layer thickness is represented by the fractions of d ; i.e. $d_1 = c_1 d$ and $d_2 = c_2 d$; where c_1 and c_2 are the dimensionless and satisfying $c_1 + c_2 = 1$. This type of artificial material is inherently anisotropic in nature. Additionally, selection of permittivity of materials $\varepsilon_1, \varepsilon_2$ and the coefficients c_1 and c_2 provide the degrees of freedom in designing required complex medium based on applications. The periodicity d of the layered MM has to be much smaller than the operating wavelength, such that the incident EM

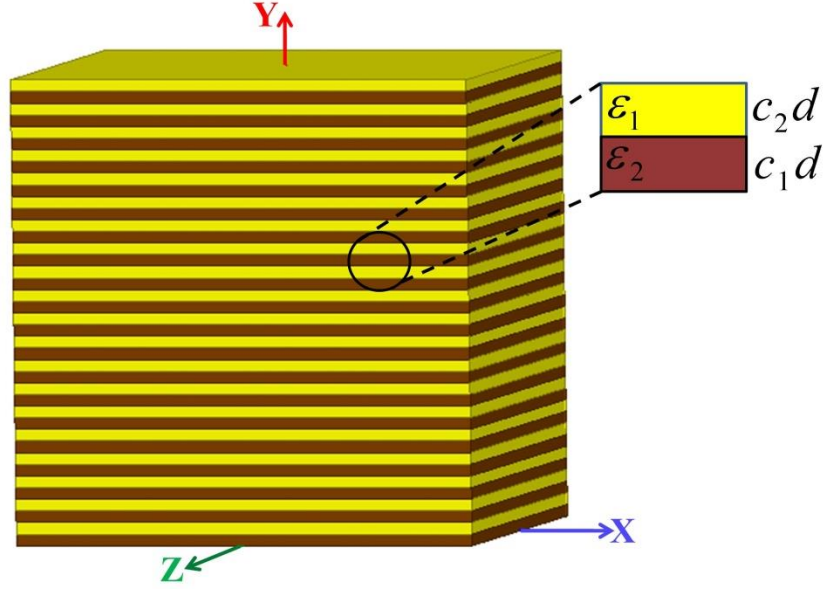


Fig. 3.10. Schematic structure of the metamaterial crystal. In the inset the various parameters are shown.

waves should see it as a homogeneous effective medium rather than a multilayer system.

Considering the periodicity along y-axis (perpendicular to the graphene plane), the permittivity tensor of the anisotropic MM can be represented as

$$\bar{\varepsilon} = \varepsilon_0 \begin{bmatrix} \varepsilon_T & 0 & 0 \\ 0 & \varepsilon_L & 0 \\ 0 & 0 & \varepsilon_T \end{bmatrix} \quad (3.6)$$

$$\text{with } \varepsilon_T = c_1\varepsilon_1 + c_2\varepsilon_2 \text{ and } \varepsilon_L = \frac{\varepsilon_1\varepsilon_2}{c_1\varepsilon_2 + c_2\varepsilon_1}$$

where ε_T and ε_L represent the transvers and longitudinal permittivity of the anisotropic MM respectively. This structure has been extensively studied by several groups for different purpose, where the stirring electromagnetic peculiarities have been traced, and paramount behavior while $\text{Sign}(\varepsilon_L) \neq \text{Sign}(\varepsilon_T)$ have been scrutinized thoroughly [104-107].

Considering the feasibility of our structure, HfO₂ film and a single layer of graphene have chosen to frame the unit cell of MM. The standard mathematical model of HfO₂ permittivity,

ϵ_{HfO_2} in 1550nm wavelength window is used [111]. The well-known Kubo's formula [112] as describe in equation 2.1 is chosen to replicate the single layer graphene permittivity.

The conductivity predicted by equation 3.6 can be converted into an in-plane complex permittivity: $\epsilon_{GR}^{\parallel} = 1 - j\sigma / (\omega\epsilon_0\delta_g)$, where ϵ_0 is the free space permittivity, and $\delta_g = 0.34nm$ is the thickness of monolayer graphene.

Single layer graphene itself is an anisotropic material whose relative permittivity in the transversal directional (on the graphene plane) $\epsilon_{GR}^{\parallel}$ follows the kobo's formula, while the permittivity perpendicular to the plane, ϵ_{GR}^{\perp} , is unity. $\epsilon_{GR}^{\parallel}$ can be tuned by charge doping or changing chemical potential through externally applied voltage. This provides mechanisms of tuning ϵ_T of the proposed MM. The real and the imaginary parts of $\epsilon_{GR}^{\parallel}$ at 1550 nm wavelength as the function of its chemical potential are shown in figure 3.11.

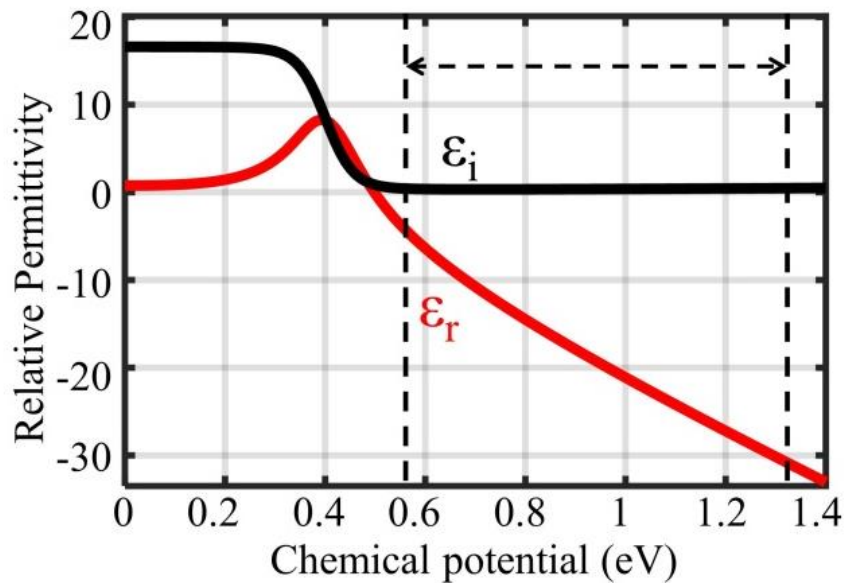


Fig. 3.11. Single layer graphene permittivity at 1550 nm wavelength as the function of chemical potential

It is evident from figure 3.11 that within the chemical potential range from 0.57eV to 1.32eV as marked by two vertical dashed lines, the imaginary part of $\epsilon_{GR}^{\parallel}$ is nearly zero and remains almost invariant, while the real part of $\epsilon_{GR}^{\parallel}$ becomes more negative with the increase of chemical potential. To achieve such a high level of chemical potential, a high electric field is needed that requires the dielectric material to have high electrical breakdown field, E_{bd} . Normally, bulk HfO₂ has low E_{bd} (lower than 1MV/cm) but when its thickness goes down to nanometer scale, E_{bd} goes abruptly high and attains a breakdown electric field as high as $E_{bd} \approx 60MV/cm$ [113]. The breakdown of nanometer-thick HfO₂ film is most likely initiated by bond rupturing rather than punctual defects as happens in bulk HfO₂ [113].

In our modeling of MM, the design parameters are taken as periodicity $d = 3nm$, $d_1 = 0.34nm$ for single layer graphene, and $d_2 = 2.66nm$ for HfO₂ film. Following the permittivity tensor of Equation 1 for anisotropic metamaterial, ϵ_T and ϵ_L can be represented as

$$\begin{aligned}\epsilon_T &= c_1 \epsilon_{GR}^{\parallel} + c_2 \epsilon_{HfO_2} \\ \epsilon_L &= \frac{\epsilon_{GR}^{\perp} \epsilon_{HfO_2}}{c_1 \epsilon_{HfO_2} + c_2 \epsilon_{GR}^{\perp}}\end{aligned}\tag{3.7}$$

where, $c_1 = 0.11333, c_2 = 0.88667, \epsilon_{GR}^{\perp} = 1$ with $\epsilon_{GR}^{\parallel}$ and ϵ_{HfO_2} can be obtained from standard formula as mention previously. It is clear from equation 3.7 that only ϵ_T will change with the variation of chemical potential. Considering the design parameters and the thickness of HfO₂ layer, an external voltage tuning from 1.1V to 6V is required to change the chemical potential of graphene from 0.57 eV to 1.32 eV. Within this voltage range maximum electric field strength inside the

dielectric layer will be 23MV/cm which is still less than half of the HfO_2 breakdown field of HfO_2 at nanometer thickness.

3.4.2 Device configuration and operation principle

The schematic diagram of the proposed MM assisted photonic coupler (hyper-coupler) is shown in figure 3.12 which is based on silicon ridge waveguides fabricated on silicon-on-insulator (SOI) wafer. Both waveguides (as denoted by WG_1 and WG_2) have identical cross-section of $420\text{nm} \times 300\text{nm}$, and they are far apart from each other except for coupling region. At the coupling region of length $5\mu\text{m}$, the separation between the two waveguides is 90nm and is filled with the anisotropic MM as described earlier.

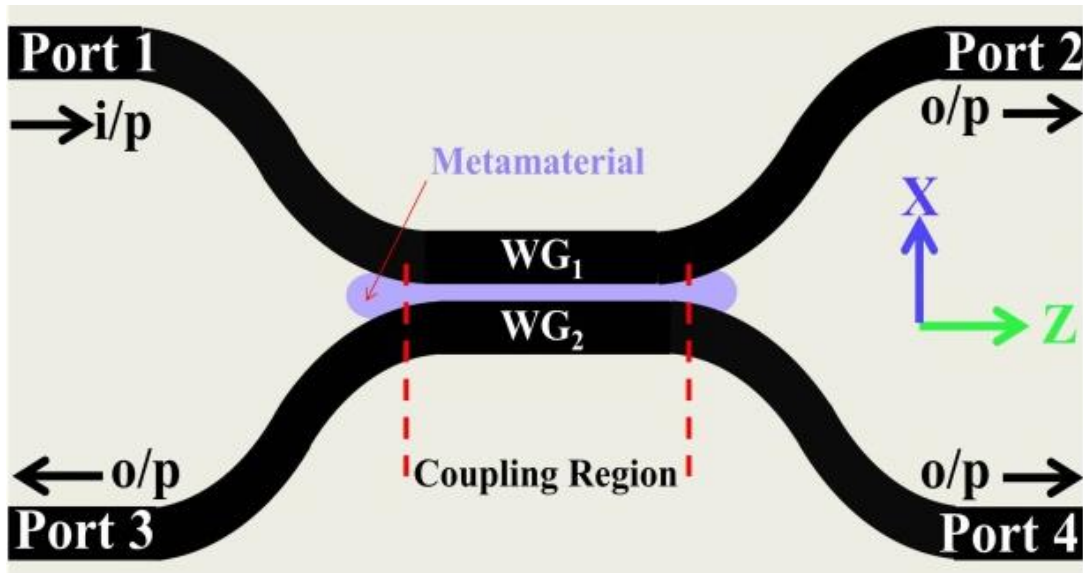


Fig. 3.12. Schematic diagram of metamaterial assisted photonic coupler based on silicon ridge waveguides.

Because of the evanescent field coupling between two waveguides, the power will transfer back and forth between waveguides along the coupling region, and the coupling coefficient can be modeled by the well-known Couple Mode Theory [22],

$$\kappa = \frac{\omega \varepsilon_0 \int_{-\infty}^{\infty} \int_{-\infty}^{\infty} (N^2 - N_2^2) \mathbf{E}_1^* \cdot \mathbf{E}_2^* dx dy}{\int_{-\infty}^{\infty} \int_{-\infty}^{\infty} \mathbf{u}_z \cdot (\mathbf{E}_1^* \times \mathbf{H}_1 + \mathbf{E}_1 \times \mathbf{H}_1^*) dx dy} \quad (3.8)$$

where, N^2 and N_2^2 are space dependent permittivity profile of the complete system and a single waveguide respectively. From the cross-sectional point of view i.e. XY-plane, both waveguides are symmetric along vertical axis (y-axis); therefore, their space dependent permittivity function will be mirror image along the same axis. \mathbf{E}_1 , \mathbf{H}_1 and \mathbf{E}_2 , \mathbf{H}_2 are the space dependent electric fields and magnetic fields distribution of WG₁ and WG₂ and * represents the complex conjugate of the vector field. ω and ε_0 represent angular frequency of operating wavelength and the vacuum permittivity respectively.

3.4.3 Results and discussion

Consider the x-polarized fundamental mode supported by the waveguides at 1550 nm wavelength, and port 1 is chosen as the input port in our simulation model as shown in figure 3.12. To characterize the proposed MM assisted coupler, two-dimensional (2D) finite-element-method (FEM) based solver (the software package COMSOL Multiphysics) is used. As our proposed design is a directional coupler, the output power from port 3 is ideally zero. The total power will split between port 2 and port 4. Due to the presence of MM between two waveguides in the coupling region which creates inhomogeneity from surrounding air, there will be a few percentage (<10%) of scattering loss in our design within the concerned range of chemical potential. Therefore, $P_2 + P_4 < P_{in}$, where P_2 and P_4 are the output powers from port 2 and port 4, respectively, with P_{in} the input power into port 1.

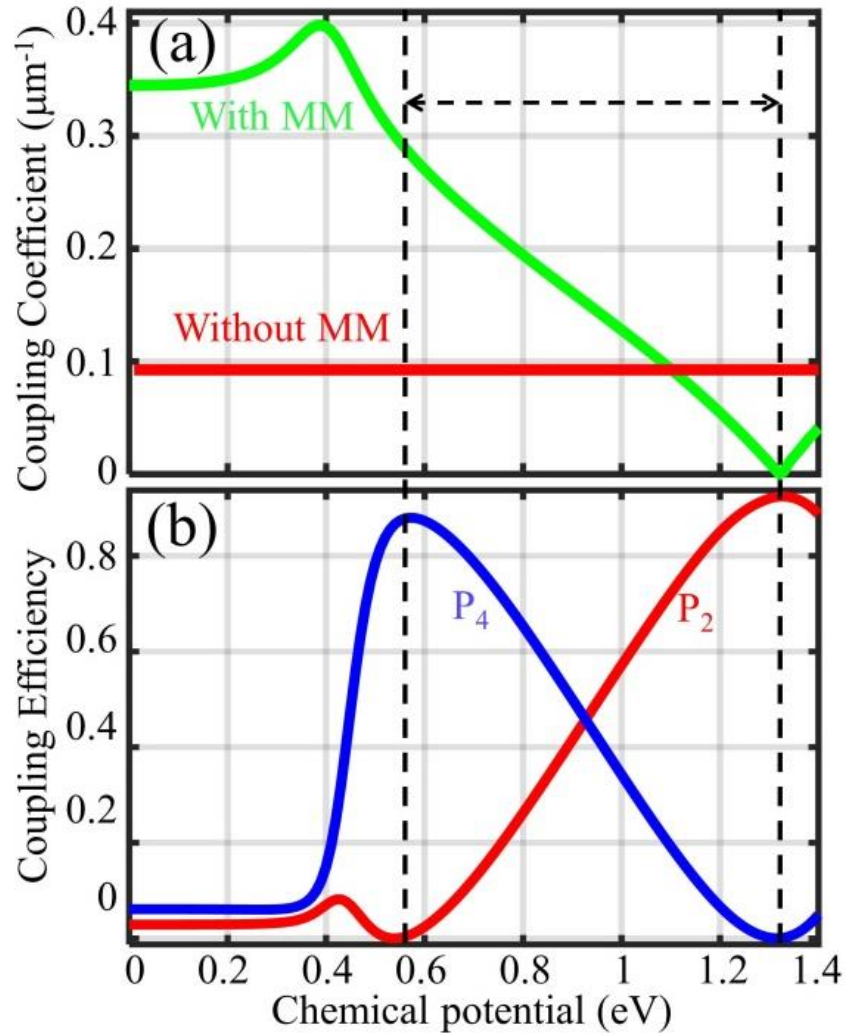


Fig. 3.13. (a) Coupling coefficient of the coupler with and without metamaterial in coupling region and (b) Normalized power output from port 2 and port 4 in terms of coupling efficiency as a function of chemical potential

In the absence of MM and considering surrounding medium as air, the coupling coefficient at 1550 nm wavelength for x-polarized fundamental mode of the designed structure is $\sim 0.0926/\mu\text{m}$, corresponding to a coupling length of approximately $17 \mu\text{m}$. Figure 3.13(a) showed that after incorporating MM in the gap between the two waveguides in the coupling region, coupling coefficient has enhanced by more than 3 times at 0.57eV chemical potential, which reduces the device size by the same factor. The power output from port 2 (P_2) and port 4 (P_4) are

shown in figure 3.13(b) which are normalized by the input power from port 1 (P_{in}). It is prominent from figure 4 that within the chemical potential range from 0.57eV to 1.32eV, the coupling coefficient reduces monotonically, and the optical signal completely switches from port 4 to port 2. Below 0.57 eV chemical potential, even though the coupling coefficient is high, the coupling efficiency is very low because the MM is lossy in this region. The normalized modal fields for ‘Even’ and ‘Odd’ modes at the cross-section of coupling region are shown in figure 3.14 for chemical potential of 0.57eV and 1.32 eV. The arrow stream indicates the field polarization of the modes.

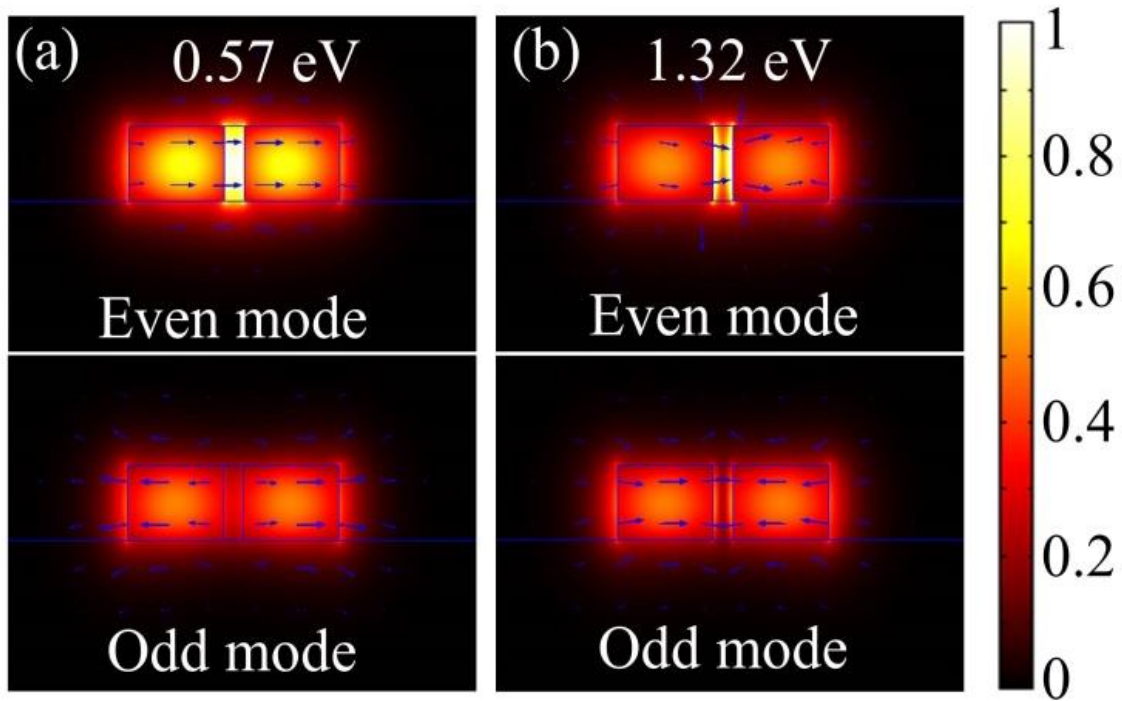


Fig. 3.14. Normalized even and odd modal electric fields with polarization indicated by arrow streamed line at chemical potential of (a) 0.57eV and (b) 1.32 eV.

Normalized electric field profiles of beam propagation through the proposed structure for two extreme points of chemical potential are shown in figure 3.15. At 0.57 eV chemical potential, almost all the power from WG_1 coupled to WG_2 because of high coupling coefficient. Whereas

at 1.32 eV chemical potential, coupling coefficient is very low so that most of the power remains confined in WG_1 and emerges from output port 2. Within the range of chemical potential between 0.57eV and 1.32eV, the monotonic change in coupling efficiency offers the capability of not only digital switching but also analog modulation of the output power between the two output ports through the modulation of the chemical potential, equivalent to a range of biasing voltage between 1.1V and 6V in this example.

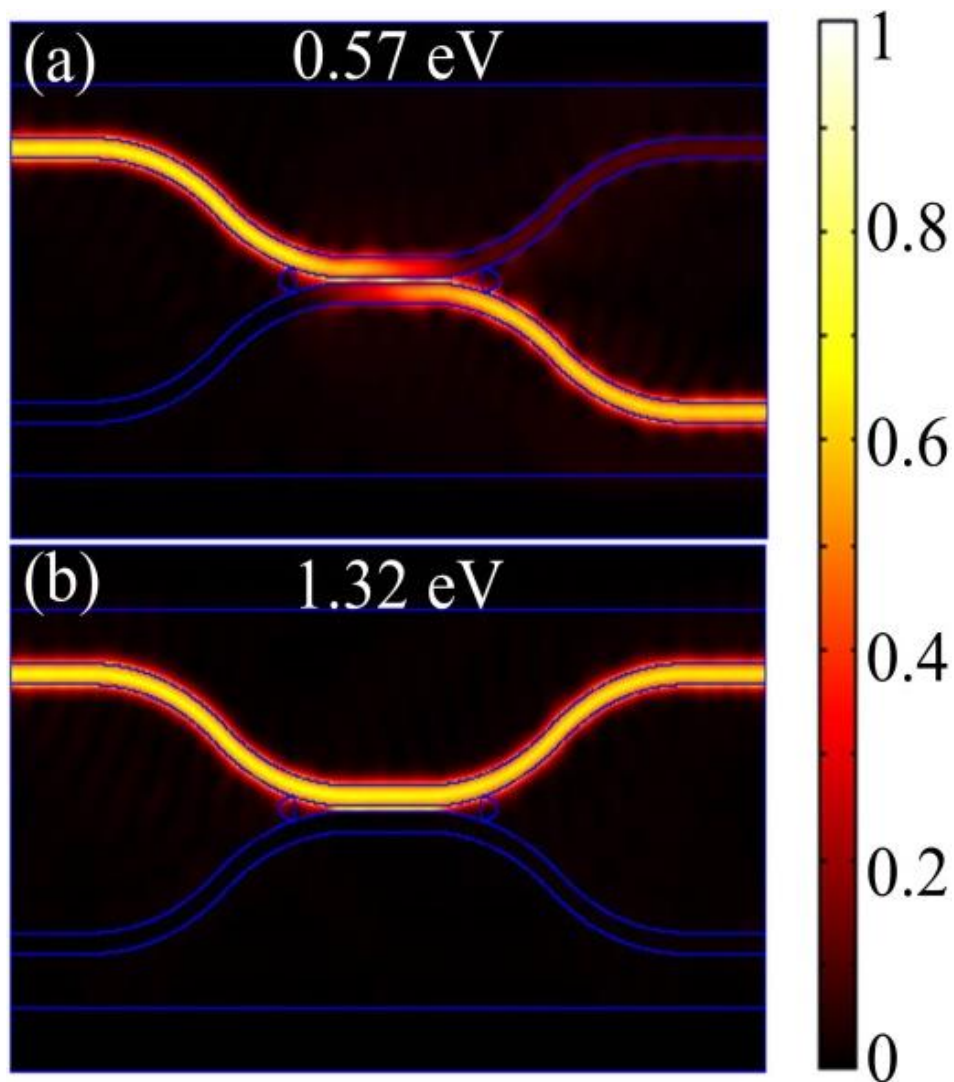


Fig. 3.15. Normalized electric field plot at chemical potential of (a) 0.57eV and (b) 1.32 eV.

3.5. Conclusion

We have proposed a highly efficient electro-optic modulation mechanism based on plasmonic graphene for applications in NIR optical communications wavelength. ITO is used to produce plasmon resonance at the NIR wavelength, and the interaction between optical field and monolayer graphene is significantly enhanced by the plasmonic effect. Tuning of graphene chemical potential through electrical gating switches on and off the ITO plasmonic resonance, providing much increased electro-optic efficiency compared to only relying on the tunable absorption of the graphene. This mechanism enables the design of electro-absorption modulators with significantly reduced size and intrinsic capacitance, critical for integrated photonic circuits with high-speed operation and low power consumption.

We have also introduced the theory and explained the physical principles of operation of modal dichroism in optical and electromagnetic waveguides. We have shown that by exploiting modal degrees of freedom the functionality-per-area in integrated photonics can be increased. Such design principles have been applied to a mode-multiplexed nanophotonic modulator. The proposed SOI device relies on the tunable modal dichroism provided by a patterned ITO film in a triple MOS capacitor arrangement. Different devices may be conceived: while in this Letter we concentrated on a nanophotonic modulator, the same structure could serve as mode converter by applying an asymmetric bias among the three ITO bars. The proposed design principles based on either polarization orthogonality or reduced modal overlap can be easily extended to other waveguide configurations, frequencies of operation, physical mechanisms of modulation, and number of modes. The possibility of selective modulation of two (or more) orthogonal modes within the same structure effectively doubles (or possibly multiplies) the functionality per area

that can be achieved. The proposed design principles can pave the way to the realization of densely integrated photonic and optoelectronic architectures.

A theoretical investigation was carried out on the properties of uniaxial MM composed of periodically stacked mono-layer graphene and nanometer-thick HfO₂ in the 1550nm optical communications wavelength. As the in-plane permittivity of mono-layer graphene ($\epsilon_{GR}^{\parallel}$) can be tuned via externally applied voltage, the anisotropic permittivity of this artificial MM along the transverse direction (ϵ_T) is also tunable. We have demonstrated that by inserting this artificial MM between two silicon ridge waveguides in the coupling region of a directional coupler, the coupling efficiency can be efficiently tuned. Our numerical simulations indicate that a complete power switch between the two output ports can be accomplished by the change of chemical potential between 0.57eV and 1.32eV. Thanks to the anomalously high breakdown field of nanometer-thick HfO₂ film, the required chemical potential on graphene is achievable.

Chapter IV:

Conclusion and future work

Never ending demand of sophisticated optical devices for integrated applications catches a great attention of the scientific societies. In terms of speed enhancement, low loss and compactness, electrical domain has over taken by the optical domain. But the bridge between these two domains is mostly taken care by the electro-optic devices, where the necessities of conversion from electrical signal to optical signal and vice versa are achievable. Electro-optic modulator is one of the devices which directly encoded electrical signal into optical carrier signal. To develop and design sophisticated electro-optic modulator, finding out the proper material or creating artificial material is highly essential.

In this dissertation, the goal is to understand the behavior of electromagnetic fields at different mediums such as dielectric medium, metallic medium, and metal-dielectric interface with different externally tunable parameters like temperature, voltage etc. Based on the electromagnetic properties and the capacity of tuning, few strategies re shown to implement them for designing different electro-optic devices. Our research findings can be summarized as follows:

1. A thorough study of reflectivity variation across the edge of CVD graphene on a SiO₂ (90 nm)/Si substrate was carried out theoretically and experimentally at 1550 nm optical communications wavelength. A theoretical prediction of phase change from 200 nm VO₂ film on a sapphire substrate was conducted with the experimentation at different pump

pulse durations at 1550 nm wavelength. Theoretical predictions of tunability of those materials are highly correlated with the experimental results. We also theoretically predicted

2. New strategies to develop highly efficient electro-optic modulation mechanism based on plasmonically enhancement of field interaction with graphene, and the permittivity tuning of ITO; for integrated applications in NIR optical communications wavelength are theoretically proposed. Doped ITO is used to enhance the interaction between optical field and monolayer graphene by producing plasmon resonance at the NIR wavelength. Tuning of graphene chemical potential through external electrical gating by switching on and off the ITO plasmonic resonance, provides higher electro-optic efficiency compared to only relying on the tunable absorption of the graphene. Similarly, exploiting the permittivity of lightly doped ITO under the application of external voltage, a tunable absorption mechanism can be achievable. Cleverly patterned ITO film in a triple MOS capacitor arrangement on SOI device provides the tunable modal dichroism. Such design principles have been applied to a mode-multiplexed nanophotonic modulator with enhancement of functionality per area.

A theoretically proposal of tunable uniaxial MM composed of periodically stacked monolayer graphene, and nanometer-thick HfO_2 and its application in the 1550nm optical communications wavelength were sketched here. As the in-plane permittivity of monolayer graphene ($\epsilon_{GR}^{\parallel}$) can be tuned via externally applied voltage, the anisotropic permittivity of this artificial MM along the transverse direction (ϵ_T) is also tunable. Based on tunable transversal permittivity of artificial MM, the coupling efficiency of

parallel waveguide coupler can be efficiently tuned at telecommunication wavelength 1550 nm. Our numerical simulations indicate that a complete power switch between the two output ports can be accomplished by the change of chemical potential between 0.57eV and 1.32eV.

There are many research opportunities looking ahead in this area of nano-photonic devices.

1. Novel photonic structure with miniature footprint is critically important to enable future large scale photonic integration. Efficient interaction between guided optical field and tunable 2-D materials through plasmonic near field enhancement has attracted considerable interest in recent years. The exploration of innovative photonic structural design through theoretical analysis and numerical modeling can be developed.
2. Additionally, research on different tunable material such as 2-D material (graphene, MoS₂), TCO, ENZ materials, and VO₂ will be continued. To make the photonic devices more efficient and smaller in size, implementation of those materials will be done into the novel photonic structure for achieving plasmonic effect. Currently the operational wavelength region is NIR region which is basically the optical communication window. A progress to extend the operational wavelength region from NIR to terahertz region is also a large area to explore [114-121].

References

- [1] M. J. Kobrinsky, B. A. Block, J.-F. Zheng, B. Barnett, E. Mohammed, M. Reshotko, F. Robertson, S. List, I. Young, and K. Cadien, "On-chip optical interconnects," *Intel Technol. J.*, vol. **8**, no. 2, pp. 129–142, May 2004.
- [2] W. Green, S. Assefa, A. Rylyakov, C. Schow, F. Horst, Y. Vlasov, SEMICON 2010.
- [3] S. Assefa, W. Green, A. Rylyakov, C. Schow, F. Horst, Y. Vlasov, OMM6, OFC 2010.
- [4] J. Van Campenhout, W. M. J. Green, S. Assefa, and Y. A. Vlasov, "Integrated NiSi waveguide heaters for CMOS-compatible silicon thermo-optic devices" *Optics Letters*, vol. **35** (7), 1013-1015 (2010).
- [5] J. Van Campenhout, W. M. J. Green, S. Assefa, and Y. A. Vlasov, "Low-power, 2×2 silicon electro-optic switch with 110-nm bandwidth for broadband reconfigurable optical networks" *Optics Express*, vol. **17**(26), 24020-24029 (2009).
- [6] S. Assefa, , Fengnian Xia , , William M. J. Green , , Clint L. Schow, Alexander V. Rylyakov, and Yurii A. Vlasov, " CMOS-Integrated Optical Receivers for On-Chip Interconnects " *IEEE Journal of Selected Topics in Quantum Electronics*, vol. **16**(5) 1376- 1385 (2010).
- [7] S. Assefa, F. Xia, S. W. Bedell, Y. Zhang, T. Topuria, P. M. Rice, and Y. A. Vlasov., "CMOS-integrated high-speed MSM germanium waveguide photodetector" *Optics Express*, vol. **18**(5), 4986-4999 (2010).
- [8] V. R. Almeida, R. Panepucci, and M. Lipson, "Compact mode conversion for highly-confined waveguides," *Integrated Photonics Research (IPR) Conference*, paper IMD 5-1, pp. 230-233, Washington 2003.

- [9] A.Liu , R. Jones, L. Liao, D. S. Rubio, D. Rubin, O. Cohen, R. Nicolaescu & M. Paniccia, “A high-speed silicon optical modulator based on a metal–oxide–semiconductor capacitor” *Nature* vol **427**, pp. 615-618, 2004.
- [10] Q. Xu, B.Schmid, S. Pradhan, and M. Lipson, “Micrometer-scale silicon electro-optic modulator,” *Nature*, vol. **435**, pp.325-327, 2005.
- [11] Q. Xu, S. Manipatruni, B. Schmidt, J. Shakya, and M. Lipson, “12.5Gbit/s carrier-injection-based silicon micro-ring silicon modulators,” *Optics express*, vol. **15**, pp. 430-436, 2007.
- [12] B. Richards and E. Wolf, “Electromagnetic Diffraction in Optical Systems. II. Structure of the Image Field in an Aplanatic System,” *Proceedings of the Royal Society of London. Series A, Mathematical and Physical Sciences*, vol. **253**, No. 1274, pp. 358-379, 1959
- [13] O. Scherzer, “The Theoretical Resolution Limit of the Electron Microscope” *Journal of Applied Physics* vol. **20**, pp. 20-29 (1949);
- [14] P. K. Ties, “Integrated optics and new wave phenomena in optical waveguides”, *Reviews of Modern Physics*, vol. **49**, No. 2, pp. 361-408, 1977
- [15] Dmitri K. Gramotnev¹ & Sergey I. Bozhevolnyi² , “Plasmonics beyond the diffraction limit,” *Nature Photonics* , vol. **4**, pp. 83 - 91 , 2010.
- [16] A.D. W. L. Barnes and T. W. Ebbesen, “Surface plasmon subwavelength optics”, *Nature*, vol. **424**, pp.824 (2003).
- [17] P. B. Johnson and R. W. Christy, “Optical constants of the noble metals,” *Phys. Rev. B*, vol. **6**, 4370 (1972).
- [18] E. D. Palik, ed., *Handbook of optical constants of solid II* , Academic Press, 1991.

- [19] P. G. Etchegoin, E. C. L. Ru, and M. Meyer, "An analytic model for the optical properties of gold," *J. Chem. Phys.* vol. **127**, 164705 (2007).
- [20] D. Marcuse, *Theory of dielectric Optical waveguides*. New York: Academic Press. 1974.
- [21] M. Born, and E. Wolf, *Principles of Optics*. Oxford: Pergamon Press. 1970.
- [22] K. Okamoto, *Fundamental of Optical Waveguides* (2nd eddition), Academic Press, 2006.
- [23] J. D. Jackson, *Classical Electrodynamics* 3rd Edition ,Wiley, 1998.
- [24] S. A. Maier, *Plasmonics : Fundamentals and applications* , Springer, 2007.
- [25] R. H. Ritchie, "Plasma losses by fast electrons in thin films," *Phys. Rev.* vol. **106**, pp. 874 , 1957.
- [26] J. M. Pitarke, V. V. Silkin, E. Chulkov, and P. Echenique, "Theory of surface plasmons and surface-plasmon polaritons," *Reports on Progress in Physics*, vol. **70**, PP. 1, 2007.
- [27] C. F. Bohren, D. R. Huffman, *Absorption and Scattering of Light by Small Particles*, Wiley-Interscience Publication, 1998.
- [28] A. Melikyan, N. Lindenmann, S. Walheim, P. M. Leufke, S. Ulrich, J. Ye, P. Vincze, H. Hahn, Th. Schimme, C. Koos, W. Freude, and J. Leuthold, "Surface plasmon polariton absorption modulator," *Optics Express*, Vol. **19**(9), 8855-8869 (2011).
- [29] Volker J. Sorger, Norberto D. Lanzillotti-Kimura, Ren-Min Ma, and Xiang Zhang, "Ultra-compact silicon nanophotonic modulator with broadband response," *Nanophotonics*. Vol **1**, Issue 1, PP 17–22 (2012).
- [30] Zhaolin Lu, Wangshi Zhao, and Kaifeng Shi, "Ultracompact Electroabsorption Modulators Based on Tunable Epsilon-Near-Zero-Slot Waveguides" *IEEE Photonics Journal*, Vol. **4** (3), PP. 735-740 (2012).

- [31] Viktoriia E. Babicheva, Andrei V. Lavrinenko, “Plasmonic modulator optimized by patterning of active layer and tuning permittivity,” *Optics Communications*, Vol. **285**, 5500-5507 (2012).
- [32] Alok P. Vasudev, Ju-Hyung Kang, Junghyun Park, Xiaoge Liu, and Mark L. Brongersma, “Electro-optical modulation of a silicon waveguide with an “epsilon-near-zero material,” *Optics Express* Vol. **21** (22), PP. 26387-26397 (2013).
- [33] Shiyang Zhu, G. Q. Lo, and D. L. Kwong, “Design of an ultra-compact electro-absorption modulator comprised of a deposited TiN/HfO₂/ITO/Cu stack for CMOS backend integration,” *Optics Express* Vol. **22** (15), PP. 17930-179347 (2014).
- [34] Jin Tae Kim, “Silicon Optical Modulators Based on Tunable Plasmonic Directional Couplers,” *IEEE Journal of Selected Topics in Quantum Electronics*, Vol. **21**(4), PP. 3300108 (2015).
- [35] Tomohiro Amemiya, Eijun Murai, Zhichen Gu, Nobuhiko Nishiyama, and Shigehisa Arai, “GaInAsP/InP-based optical modulator consisting of gap-surface-plasmon-polariton waveguide: theoretical analysis,” *J. Opt. Soc. Am. B*, Vol. **31**(11), PP. 2908-2913 (2014).
- [36] Hongwei Zhao, Yu Wang, Antonio Capretti, Luca Dal Negro, and Jonathan Klamkin, “Broadband Electroabsorption Modulators Design Based on Epsilon-Near-Zero Indium Tin Oxide,” *IEEE Journal of Selected Topics in Quantum Electronics*, Vol. **21**(4), PP. 3300207 (2015).
- [37] J. Horng, C.-F. Chen, B. Geng, C. Girit, Y. Zhang, Z. Hao, H. A. Bechtel, M. Martin, A. Zettl, M. F. Crommie, Y. R. Shen, and F. Wang, “Drude conductivity of Dirac fermions in graphene” *Physical Review B*, vol. **83**, 165113 (2011).

- [38] F. Wang, Y. Zhang, C. Tian, C. Girit, A. Zettl, M. Crommie, and Y. R. Shen, "Gate-Variable Optical Transitions in Graphene," *Science*, vol. **320**, 206-209 (2008).
- [39] Y.-M. Lin, C. Dimitrakopoulos, K. A. Jenkins, D. B. Farmer, H.-Y. Chiu, A. Grill, and Ph. Avouris, "100-GHz Transistors from Wafer-Scale Epitaxial Graphene" *Science*, vol. **327**, 662 (2010)
- [40] F. Schedin, A. K. Geim, S. V. Morozov, E. W. Hill, P. Blake, M. I. Katsnelson and K. S. Novoselov, "Detection of individual gas molecules adsorbed on graphene" *Nature Materials*, vol. **6**, 652 - 655 (2007)
- [41] L. Ju, B. Geng, J. Horng, C. Girit, M. Martin, Z. Hao, H. A. Bechtel, X. Liang, A. Zettl, Y. R. Shen and F. Wang, "Graphene plasmonics for tunable terahertz metamaterials" *Nature Nanotechnology*, vol. **6**, 630–634 (2011)
- [42] M. Liu, X. Yin, E. Ulin-Avila, B. Geng, T. Zentgraf, L. Ju, F. Wang and X. Zhang, "A graphene-based broadband optical modulator" *Nature*, vol. **474**, 64-67 (2011)
- [43] Z. Lu and W. Zhao, "Nanoscale electro-optic modulators based on graphene-slot waveguides" *JOSA B*, vol. **29**, 1490-1496 (2012)
- [44] L. Yang, T. Hu, A. Shen, C. Pei, B. Yang, T. Dai, H. Yu, Y. Li, X. Jiang, and J. Yang, "Ultracompact optical modulator based on graphene-silica metamaterial" *Opt. Lett.*, vol. **39**, 1909-1912 (2014)
- [45] X. Wang, Y. P. Chen and D. D. Nolte, "Strong anomalous optical dispersion of graphene: complex refractive index measured by Picometrology" *Optics Express*, vol. **16**, 22105 (2008)
- [46] G. W. Hanson, "Dyadic Green's functions and guided surface waves for a surface conductivity model of graphene" *J. Appl. Phys.*, vol. **103**, 064302 (2008)

- [47] C. Hwang, D. A. Siegel, S.-K. Mo, W. Regan, A. Ismach, Y. Zhang, A. Zettl, and Alessandra Lanzara, "Fermi velocity engineering in graphene by substrate modification," *Scientific Reports*, vol. **2**, 590 (2012)
- [48] Y. G. Lee, C. G. Kang, U. J. Jung, J. J. Kim, H. J. Hwang, H.-J. Chung, S. Seo, R. Choi, and B. H. Lee, "Fast transient charging at the graphene/SiO₂ interface causing hysteretic device characteristics," *Appl. Phys. Lett.* vol. **98**, pp. 183508 (2011).
- [49] H. Kalita, V. Harikrishnan, D. B. Shinde, V. K. Pillai, and M. Aslam, "Hysteresis and charge trapping in graphene quantum dots," *Appl. Phys Lett*, vol. **102**, 143104 (2013)
- [50] G. V. Naik, V. M. Shalaev, and A. Boltasseva, "Alternative Plasmonic Materials: Beyond Gold and Silver," *Advanced Materials*, vol. **25**, pp. 3264-3294, 2013.
- [51] E. Feignbaum, K. Diest, and H. A. Atwater, "Unity-Order Index Change in Transparent Conducting Oxides at visible Frequencies," *Nano Letters*, vol. **10**, pp. 2111-2116, 2010
- [52] Xu, Q. F. and M. Lipson , "All-optical logic based on silicon micro-ring resonators." *Optics express*. vol. **15**(3), pp. 924-929. (2007).
- [53] Liu, A., et al., "A high-speed silicon optical modulator based on a metal–oxide–semiconductor capacitor." *Nature*, vol. **427**(6975), pp. 615-618. (2004).
- [54] Q. Xu, et al. "Micrometre-scale silicon electro-optic modulator." *Nature*, vol. **435**(7040): 325-327., (2005).
- [55] Ryckman, J. D., et al. "Ultra-compact silicon photonic devices reconfigured by an optically induced semiconductor-to-metal transition." *Optics express*, vol. **21**(9): 10753-10763., (2013).

- [56] Kim, H., et al., "Optimization of the semiconductor-metal transition in VO₂ epitaxial thin films as a function of oxygen growth pressure." *Applied Physics Letters*, vol. **104**(8): 081913., (2014).
- [57] Nag, J. and R. Haglund Jr, "Synthesis of vanadium dioxide thin films and nanoparticles." *Journal of Physics: Condensed Matter*, vol. **20**(26): 264016., (2008).
- [58] Petrov, G., et al., "Nonlinear optical microscopy analysis of ultrafast phase transformation in vanadium dioxide." *Optics letters*, vol. **27**(8): 655-657., (2002).
- [59] Cavalleri, A., et al., "Femtosecond structural dynamics in VO₂ during an ultrafast solid-solid phase transition." *Physical Review Letters*, vol. **87**(23), pp. 237401., (2001).
- [60] Kim, H.-T., et al., "Raman study of electric-field-induced first-order metal-insulator transition in VO₂-based devices." *Applied Physics Letters*, vol. **86**(24): 242101-242101, (2005).
- [61] Cavalleri, A., et al., "Evidence for a structurally-driven insulator-to-metal transition in VO₂: A view from the ultrafast timescale." *Physical Review B*, vol. **70**(16): 161102., (2004).
- [62] Briggs, R. M., et al., "Compact silicon photonic waveguide modulator based on the vanadium dioxide metal-insulator phase transition." *Optics express*. Vol. **18**(11): 11192-11201., (2010).
- [63] Choi, J. M., et al., "Control of critical coupling in a ring resonator–fiber configuration: application to wavelength-selective switching, modulation, amplification, and oscillation." *Optics letters*, vol. **26**(16): 1236-1238., (2001).
- [64] Son, T., et al., "Pure optical phase control with vanadium dioxide thin films." *Optics Communications*, vol. **320**: 151-155., (2014).

- [65] Joushaghani, A., et al., "Wavelength-size hybrid Si-VO₂ waveguide electroabsorption optical switches and photodetectors." *Optics express*, vol. **23**(3): 3657-3668., (2015).
- [66] Kim, J. T., "CMOS-compatible hybrid plasmonic modulator based on vanadium dioxide insulator-metal phase transition." *Optics letters*, vol. **39**(13): 3997-4000., (2014).
- [67] K.S. Novoselov, A.K. Geim, S. Morozov, D. Jiang, Y. Zhang, S. Dubonos, I. Grigorieva, A. Firsov, Electric field effect in atomically thin carbon films, *Science*, vol. **306** (2004) 666-669.
- [68] Y.-M. Lin, C. Dimitrakopoulos, K. A. Jenkins, D. B. Farmer, H.-Y. Chiu, A. Grill, and Ph. Avouris, "100-GHz Transistors from Wafer-Scale Epitaxial Graphene" *Science*, vol. **327** 662 (2010)
- [69] L. Britnell, et al., "Field-Effect Tunneling Transistor Based on Vertical Graphene Heterostructures," *Science*, vol. **335**, 6071 (2012)
- [70] Gan, X. et al. "Chip-integrated ultrafast graphene photodetector with high responsivity," *Nature Photon.* vol. **7**, 883–887 (2013).
- [71] Pospischil, A. et al. CMOS-compatible graphene photodetector covering all optical communication bands. *Nature Photon.* vol. **7**, 892–896 (2013).
- [72] M. Liu, X. Yin, E. Ulin-Avila, B. Geng, T. Zentgraf, L. Ju, F. Wang, X. Zhang, A graphene-based broadband optical modulator, *Nature*, vol. **474** (2011) 64-67.
- [73] M. Liu, X. Yin, X. Zhang, "Double-layer graphene optical modulator", *Nano Lett.*, **12** (2012) 1482-1485.
- [74] Grigorenko, M. Polini, K. Novoselov, "Graphene plasmonics", *Nat. Photonics*, vol. **6** (2012) 749-758.

- [75] S. Thongrattanasiri, F. H. L. Koppens, and F. Javier García de Abajo, “Complete Optical Absorption in Periodically Patterned Graphene”, *Phys. Rev. Lett.* vol. **108**, 047401 (2012).
- [76] Y. Fan, Z. Wei, Z. Zhang, and H. Li, “Enhancing infrared extinction and absorption in a monolayer graphene sheet by harvesting the electric dipolar mode of split ring resonators”, *Opt Lett.* vol. **38**, 5410 (2013).
- [77] Y. Fan, N.-H. Shen, T. Koschny, and C. M. Soukoulis, “Tunable Terahertz Meta-Surface with Graphene Cut-Wires” *ACS Photonics*, vol. **2**, 151 (2015).
- [78] G. Xu, J. Liu, Q. Wang, R. Hui, Z. Chen, V.A. Maroni, J. Wu, “Plasmonic graphene transparent conductors, *Advanced Materials*”, vol. **24** (2012) OP71-OP76.
- [79] W. L. Barnes, A. Dereux and T. W. Ebbesen, "Surface plasmon subwavelength optics," *Nature* **424**, 824-830 (2003)|
- [80] R. Lu, A. Konzelmann, F. Xu, J. Liu, Q. Liu, M. Xin, R. Hui, and J. Z. Wu, “High Sensitivity Surface Enhanced Raman Spectroscopy of R6G on *in situ* Fabricated Au Nanoparticle/Graphene Plasmonic Substrates”, *Carbon*, published online January (2015),
- [81] G. V. Naik, J. Kim, and A. Boltasseva, " Oxides and nitrides as alternative plasmonic materials in the optical range," *Optical Materials Express*, **1**, 1090-1099 (2011)
- [82] R. G. Gordon, "Criteria for Choosing Transparent Conductors," *MRS Bulletin*, **25**, 52-57 (2000)
- [83] L. Liao and X. Duan, “Graphene–dielectric integration for graphene transistors” *Mater. Sci. Eng. R* vol. **70**, 354 (2010).

- [84] S. Kim, J. Nah, I. Jo, D. Shahrjerdi, L. Colombo, Z. Yao, E. Tutuc, and S. K. Banerjee, “Realization of a high mobility dual-gated graphene field-effect transistor with Al₂O₃ dielectric” *Appl. Phys. Lett.* vol. **94**, 062107 (2009).
- [85] S. Association, “The international technologyroadmap for semiconductors (ITRS),” ed, 2005.
- [86] R. Kirchain and L. Kimerling, “A roadmap for nano photonics,” *Nature Photonics*, vol. **1**, pp. 303-305, 2007.
- [87] T. Phare, Y. H. D. Lee, J. Cardenas, and M. Lipson, “Graphene electro-optic modulator with 30GHz bandwidth,”. *Nature Photonics*, vol. **9**, pp. 511-514, 2015
- [88] S. Das, A. Salandrino, J. Z. Wu, and R. Hui, “Near-infrared electro-optic modulator based on plasmonic graphene,” *Optics Letters*, vol. **40**, pp. 1516-1519, 2015.
- [89] C. Ye, S. Khan, Z. R. Li, E. Simsek, and V.J. Sorger, “1-size ITO and graphene based electro-optic modulators on SOI,” *Selected Topic in Quantum Electronics, IEEE Journal of Lightwave Technology*, vol. **20**, pp. 40-49, 2014.
- [90] J. Gosciniaak and D. T. Tan, “Graphene-based waveguide integrated dielectric-loaded plasmonic electro-absorption modulator,” *Nanotechnology*, vol. **24**, pp. 185202, 2013.
- [91] V. J. Sorger, N. D. Lanzillotti-Kimura, R. M. Ma, and X. Zhang, “Ultra-compact silicon nanophotonic modulator with broarband response,” *Nanophotonics*, vol. **1**, pp. 17-22, 2012.
- [92] W. Li, B. Chen, C. Meng, W. Fang, Y. Xiao, X. Li, Z. Hu, Y. Xu, L. Tong, and H. Wang, “Ultrafast All-Optical Graphene Modulator,” *Nano Lett.* Vol. **14**, 955 (2014).
- [93] J.-P. Colinge and C. A. Colinge, *Physics of Semiconductor Devices* (Springer, 2005).
- [94] COMSOL RF Module.

- [95] Z. Lu, K. Shi, and P. Yin, "Photonic MOS Based on "Optical Property Inversion"", *MRS Adv.* Vol. **1**, 1657 (2016).
- [96] Andrea Alù and Nader Engheta, 'Light squeezing through arbitrarily shaped plasmonic channels and sharp bends' *Physical Review B* Vol. **78**, 035440 (2008)
- [97] Ma'rio Silveirinha and Nader Engheta, 'Tunneling of Electromagnetic Energy through Subwavelength Channels and Bends using ϵ -Near-Zero Materials' *PRL* Vol. **97**, 157403 (2006)
- [98] Kan Yao and Yongmin Liu, 'Plasmonic metamaterials' *Nanotechnol Rev* Vol. **3** (2): 177–210, (2014)
- [99] S. Das, R. Halder and S. K. Varshney, "Triple-core Collinear and Non-Collinear Plasmonic Photonic Crystal Fiber Couplers", *Applied Optics*, Vol-**52**, No-34, pp-8199-8204, (2013).
- [100] C. Haffner, W. Heni1, Y. Fedoryshyn, *et.al.*, 'All-plasmonic Mach-Zehnder modulator enabling optical high-speed communication at the microscale' *Nature Photonics* Vol. **9**, 525–528 (2015).
- [101] Tiesheng Wu, Yumin Liu, Zhongyuan Yu, Yiwei Peng, Changgan Shu, and Han Ye, 'The sensing characteristics of plasmonic waveguide with a ring resonator' *Optics Express* Vol. **22**, No. 7 , 7669-7677, (2014)
- [102] Lin Chen,tian zhang,Xiang Yin,Xun Li 'Ultra-compact polarization beam splitter utilizing a graphene-based asymmetrical directional coupler' *Optics Letters* Vol. **41**, No. 2 , 356-359 , (2016).

- [103] R. Filter, M. Farhat, M. Steglich, R. Alaei, C. Rockstuhl, and F. Lederer¹ ‘Tunable graphene antennas for selective enhancement of THz-emission’ *Optics Express* Vol. **21**, No. 3, 3737-3745, (2013).
- [104] S. Anantha Ramakrishna, J. B. Pendry, M. C. K. Wiltshire, and W. J. Stewart, ‘Imaging the near field’ *J. Mod. Opt.* Vol. **50**, 1419, (2003).
- [105] S. Feng and J. Elson, ‘Diffraction-suppressed high-resolution imaging through metallodielectric nanofilms’, *Opt. Express* Vol. **14**, 216, (2006).
- [106] D. Schurig and D. R. Smith, ‘Sub-diffraction imaging with compensating bilayers’, *New J. Phys.* Vol. **7**, 162 (2005).
- [107] P. A. Belov and Y. Hao, ‘Subwavelength imaging at optical frequencies using a transmission device formed by a periodic layered metal-dielectric structure operating in the canalization regime’, *Phys. Rev. B* Vol. **73**, 113110 (2006).
- [108] S. Das, S. Fardad, I. Kim, J. Rho, R. Hui, and A. salandrino, “Nanophotonic Modal Dichroism: Mode-Multiplexed Modulators” *Optics Letters*, Vol. **41**, No. 18, pp. 4394-4397, 2016.
- [109] Pekka Alitalo, Sergei Tretyakov, ‘Electromagnetic cloaking with metamaterials’ *Materialstoday, Materialtoday*, Vol. **12**, No. 3, 2009
- [110] Alessandro Salandrino and Nader Engheta, ‘Far-field subdiffraction optical microscopy using metamaterial crystals: Theory and simulations’ *Physical Review B*, Vol. **74**, 075103 (2006)
- [111] D. L. Wood, Kurt Nassau, T. Y. Kometani, and D. L. Nash. “Optical properties of cubic hafnia stabilized with yttria”. *Appl. Opt.* Vol. **29**, 604-607 (1990)

- [112] F. Xu, S. Das, Y. Gong, Q. Liu, H. C. Chien, H. Y. Chiu, et al., "Complex refractive index tunability of graphene at 1550 nm wavelength," *Applied Physics Letters*, Vol. **106**, p. 031109, 2015.
- [113] Cédric Sire, Serge Blonkowski, Michael J. Gordon, and Thierry Baron, 'Statistics of electrical breakdown field in Hf O 2 and Si O 2 films from millimeter to nanometer length scales' *Applied Physics Letters* Vol. **91**, 242905 (2007);
- [114] Yu Yao, Mikhail A. Kats, Patrice Genevet, Nanfang Yu, Yi Song, Jing Kong, and Federico Capasso, "Broad Electrical Tuning of Graphene-Loaded Plasmonic Antennas" *Nano Lett.*, vol. **13** (3), pp 1257–1264, 2013.
- [115] Long Ju ,BaisongGeng, Jason Horng, Caglar Girit, Michael Martin, ZhaoHao , HansA.Bechtel, Xiaogan Liang, Alex Zettl, Y.RonShen, and Feng Wang, "Graphene plasmonics for tunable terahertz metamaterials:", *Nature Nanotechnology*, vol. **6**, 630–634 (2011)
- [116] Bo Zhao and Zhuomin M. Zhang, "Strong Plasmonic Coupling between Graphene Ribbon Array and Metal Gratings", *ACS Photonics*, vol. **2** (11), pp 1611–1618, 2015.
- [117] Yang Zhao and Andrea Alù, "Manipulating light polarization with ultrathin plasmonic metasurfaces", *Phys. Rev. B* vol. **84**, 205428 – Published 16 November 2011
- [118] Nanfang Yu, Patrice Genevet, Mikhail A. Kats, Francesco Aieta, Jean-Philippe Tetienne, Federico Capasso, Zeno Gaburro, "Light Propagation with Phase Discontinuities: Generalized Laws of Reflection and Refraction", vol. **334** no. 6054 pp. 333-337, *Science* 2011

- [119] Anders Pors , Michael G. Nielsen , and Sergey I. Bozhevolny, “Plasmonic metagratings for simultaneous determination of Stokes parameters”, *Optica*, vol. **2**, , Issue 8, pp. 716-723 , (2015).
- [120] Huguen Yan, Xuesong Li, Bhupesh Chandra, George Tulevski, Yanqing Wu, Marcus Freitag, Wenjuan Zhu, Phaedon Avouris & Fengnian Xia, “Tunable infrared plasmonic devices using graphene/insulator stacks”, *Nature Nanotechnology* vol. **7**, pp. 330–334 (2012).
- [121] Servin Rathi, Inyeal Lee, Dongsuk Lim, Jianwei Wang, Yuichi Ochiai, Nobuyuki Aoki, Kenji Watanabe, Takashi Taniguchi, Gwan-Hyoung Lee, Young-Jun Yu, Philip Kim, and Gil-Ho Kim, “Tunable Electrical and Optical Characteristics in Monolayer Graphene and Few-Layer MoS₂ Heterostructure devices”, *Nano Lett.*, vol. **15**, 5017–5024, 2015